united nations
educational, scientific
and cultural
organization

international atomic
energy agency

the
abdus salam
international centre for theoretical physics

SMR.1135 - 1

THIRD WORKSHOP ON
THIN FILMS PHYSICS AND TECHNOLOGY
(8 - 24 MARCH 1999)
including
TOPICAL CONFERENCE ON
MICROSTRUCTURE AND SURFACE MORPHOLOGY
EVOLUTION IN THIN FILMS
(24 - 26 MARCH 1999)

"Wear-resistant and low friction coatings: Synthesis, Characterization and Applications"

Yves PAULEAU
INPG-ENSEEG
B.P. 75
1130 Rue de la Piscine
38402 Cedex Saint Martin d'Heres
FRANCE

These are preliminary lecture notes, intended only for distribution to participants.

[illegible] www.ictp.trieste.it

WEAR-RESISTANT AND LOW FRICTION COATINGS : Synthesis, Characterization and Applications

Yves Pauleau
National Polytechnic Institute of Grenoble
ENSEEG, B.P. 75, 38402 Saint Martin d'Hères Cedex, France
Tel : (33)-4-76-82-65-25; Fax : (33)-4-76-82-66-30; E-mail : yves.pauleau@enseeg.inpg.fr

TOPICAL OUTLINE

I - Wear-Resistant Coatings

1. Introduction

II - Low Friction Coatings

1. Introduction

WEAR-RESISTANT AND LOW FRICTION COATINGS : Synthesis, Characterization and Applications

Yves Pauleau
National Polytechnic Institute of Grenoble
ENSEEG, B.P. 75, 38402 Saint Martin d'Hères Cedex, France
Tel : (33)-4-76-82-65-25; Fax : (33)-4-76-82-66-30; e-mail : yves.pauleau@enseeg.inpg.fr

ABSTRACT

The wear of materials surfaces subjected to relative motion is manifested by a loss of materials from one or both surfaces as loose particles produced by mechanical action between contacting surfaces. Common mechanisms by which material may be removed from the surface involve adhesion, abrasion, fatigue, fretting or corrosion phenomena. In some situations more than one of these wear mechanisms may be operative at the same time.

According to the Archard relation, the volume, V, of particles resulting from adhesive or abrasive wear is found to be inversely proportional to the hardness, H, of the softer material in sliding contact and proportional to both the load, W, applied to sliding contact in which adhesion or abrasion phenomena occur and the distance of sliding, L. Therefore, the hardness of materials in sliding contact appears as the major intrinsic property or factor affecting the wear resistance of materials in moving mechanical assemblies.

Furthermore, lubrication is well-known to aid in reducing wear of interacting surfaces. The factor of proportionality in the Archard relation called the wear coefficient or the Archard factor is dependent on the type of lubricants employed to reduce friction. The friction coefficient, wear and lubrication mechanisms involved in the sliding contact are related to the lubricant materials and operation conditions of mechanical assemblies (temperature, corrosion environment, ...).

Usually, hard materials suffer from a low ductility and are susceptible to brittle fracture. As a result, hard bulk materials cannot be used in many applications with high intensities of load applied to sliding contact. In such cases, a more ductile bulk material coated with a hard wear-resistant coating is used. The hardness of materials surfaces can be improved by either surface modification techniques (laser-induced surface hardening, ion implantation, carburizing or nitriding processes) or deposition of coatings via various

techniques (plasma and flame spraying, electroplating, chemical vapor deposition (CVD), physical vapor deposition (PVD)). In this lecture, we consider essentially coatings grown from the vapor phase by either PVD or CVD. In general, materials which exhibit high intrinsic hardnesses can be categorized as having high cohesive energy, short bond length and high degree of covalent bonding.

In the first part of the lecture, the existing knowledge based on results reported in the literature about relationships between the microstructure and physical properties of hard coatings is discussed. Particular emphasis is placed on the role of microstructure features such as grain boundaries, non equilibrium structures, impurities and texture in controlling the hardness of coatings. Voids and weak grain boundaries give rise to low hardnesses whereas dense coatings with a high defect concentration can have hardnesses far above bulk values. Transition metal nitrides and carbides such as TiN and TiC have achieved by far the highest level of success in numerous applications. In this lecture, a review of the hard coating literature is given and includes in addition to nitrides and carbides also metastable hard coatings, multilayer coatings, thick coatings produced by electron beam physical vapor deposition (EB-PVD) and erosion-resistant sputter-deposited W-C/W multilayer coatings.

Solid lubricant coatings are required for lubrication of moving mechanical assemblies operating in hostile environments (extreme temperatures, vacuum, corrosive atmospheres, ...) where conventional fluid lubricants fail. In the second part of the lecture, general considerations on friction between surface in unlubricated and lubricated sliding contact are presented with a particular emphasis on Amontons' law, nature of the contact and friction phenomena between two solid surfaces. The basic mechanisms of friction which involve shearing and plowing phenomena, adhesion effect on real contact area, lubrication effect of oxide films are discussed. The lubrication mechanisms by thin solid films are described on the basis of macroscopic and microscopic approaches.

Materials for solid lubricant films produced by plasma-based deposition techniques are highlighted and illustrated by various examples (molybdenum disulfide, amorphous carbon, silver, calcium fluoride films and Ag/CaF_2 multilayer films). Finally, the major factors and relevant properties of materials which can be useful to a designer selecting coating processes and coating materials for a given lubrication application are analyzed in the last section of the lecture.

Surface and Coatings Technology, 62 (1993) 474–479

Tungsten and tungsten–carbon PVD multilayered structures as erosion-resistant coatings

E. Quesnel and Y. Pauleau*
Centre d'Etudes Nucléaires de Grenoble, CEREM/DEM, 85X, 38041 Grenoble Cedex (France)

P. Monge-Cadet and M. Brun
TURBOMECA, 64511 Bordes (France)

Abstract

The aerospace industry is faced with a major erosive wear problem of engine components operating in dust environments. Various physical vapor deposition (PVD) or chemical vapor deposition (CVD) protective coatings have been used previously with limited success. The present paper deals with the elaboration and characterization of W/W–C multilayer coatings produced by magnetron sputtering from a W target in Ar and in an Ar+methane mixture respectively. This low temperature PVD process, compared with CVD processes, enables the deposition of protective coatings on Ti6Al4V substrates at temperatures below 400 °C. The microhardness of W–C films was found to be strongly dependent on the carbon concentration; two maximum hardness values of 26000 MPa were obtained with W–C layers containing either 14–15 at.% or 40–45 at.% C. This change in microhardness with the carbon content was correlated with the evolution of the crystallographic structure. Multilayer coatings of total thickness 60 μm composed of various W/W–C stacking arrangements have been elaborated with hard W–C films containing 14–15 at.% or 40–45 at.% C. These samples were subjected to erosive wear tests using a sand blast unit. As a comparison, Mo/Mo–C and Cr/Cr–C structures containing more than 10 at.% C were also tested. W/W–C coatings with an appropriate stacking arrangement and a C concentration of 14–15 at.% in W–C layers exhibited an erosion resistance improved by more than two orders of magnitude compared with that of uncoated Ti6Al4V substrates. Complementary tests of the fatigue performance of Ti6Al4V specimens coated with these very promising erosion-resistant coatings were also performed.

1. Introduction

The erosive wear of materials caused by the impingement of solid particles is a well-known industrial problem, for instance, in the case of compressor blades used in gas turbine engines in aeronautics. In this particular case, different approaches can be considered and consist of (i) filtering the air entering the compressor, which is an efficient solution but limits the engine yield, (ii) using stainless steel blades, which are approximately twice as resistant as Ti alloy blades but much heavier, or (iii) protecting the blades by an erosion-resistant coating. This last solution seems to be undoubtedly the best way, provided that the material and deposition process are compatible with the application. Therefore, with the aim of protecting Ti alloy(Ti6Al4V)-based compressor blades, in the present work, we have developed a new coating which takes into account the fact that, in real conditions, the components are submitted to sand particles impacting under a wide range of impingement angles. We also considered the necessity for the base material to keep its complete mechanical characteristics after the coating treatment.

It is indeed widely agreed that the erosion performance of materials depends on the incidence angle of particle flux. There are essentially two kinds of erosion resistance behavior [1]. One is characteristic of a ductile material, such as metals, with the best erosion resistance for an impingement angle normal to the eroded surface. The other, with the best erosion resistance for small angles of incidence, is characteristic of a brittle material.

Various materials, for instance, Cr carbide [2], Ti carbide or nitride [3] and WC [4, 5], have been studied as erosion-resistant protective coatings. Different processes, such as plasma spraying, D-gun, physical vapor deposition (PVD) and mostly chemical vapor deposition (CVD), have been used for depositing these materials.

Nevertheless, most CVD processes are carried out at temperatures above 500 °C, which does not allow the coatings to be applied to ferrous metals or Ti alloys without significantly affecting their mechanical properties and, in particular, their fatigue resistance. To overcome the substrate limitations, different kinds of WC coatings have been developed and deposited by low temperature CVD processes. For instance, the

---

*Present address: Institut National Polytechnique de Grenoble, ENSEEG, BP 75, 38402 Saint Martin d'Hères, France.

0257-8972/93/$6.00

"CM500L" coating is deposited by the controlled nucleation thermochemical deposition (CNTD) process, at temperatures ranging from 350 to 550 °C [5]. Using the same CNTD process, Dyer and coworkers [4, 6] have produced, at temperatures below 500 °C, thick W/W_xC multilayers which exhibit good erosion resistance. This stacking arrangement enables the deposition of thicker coatings and, at the same time, allows ductile and brittle materials to be combined in the same protective coating, thus promoting a better erosion resistance at any incident angle of particles.

In the present work, thick W/W–C multilayers were deposited using a low temperature PVD process. One peculiarity of this process is that the structure of the W–C material is either a WC phase or a solid-solution-type W–C phase, depending on the C concentration in the material. The erosion resistance of the multilayers was thus examined according to the nature of the W–C phase and also according to the W/W–C stacking arrangement. The fatigue performances of coated Ti6Al4V specimens were also tested.

2. Experimental procedure

The W/W–C multilayer coatings were deposited on Ti6Al4V plates 50 mm × 50 mm by a d.c. reactive magnetron sputtering method, using a planar target of pure W. The typical deposition conditions were a target–substrate distance of 7 cm, a sputtering power density of $8\ \mathrm{W\ cm^{-2}}$, a substrate bias of -100 V and a total pressure of 0.5 Pa. The temperature of the substrate was measured with a chromel–alumel thermocouple mounted on the substrate holder.

According to the deposited layer, *i.e.* either W or W–C, the sputtering gas was pure Ar or a methane + Ar mixture respectively. The elaboration of W/W–C multilayers was operated in the same deposition step; the change of single-layer material, *i.e.* from W to W–C or from W–C to W, was obtained by switching on or off the methane gas inlet in the vacuum chamber. A typical deposition run of a multilayer 60 μm thick lasted around 6 h and the maximum temperature reached by the substrate remained under 300 °C.

Mo/Mo–C and Cr/Cr–C multilayer structures 60 μm thick, used as comparison specimens for the erosion tests, were also deposited on Ti6Al4V substrates. Their deposition conditions were quite similar to those of W/W–C multilayers, the target used being pure Mo or Cr respectively [7].

To characterize the single-layer materials that compose the multilayers, preliminary coatings 5 μm thick of pure W or W–C were prepared on stainless steel substrates. The C concentration, crystallographic structure and Vickers hardness of these coatings have been analysed according to the procedure described previously [8, 9].

The erosion performance of the multilayers was determined using a sand blast unit, where the silica grit was supplied through a nozzle from a powder feeder and accelerated in an air flow. The erosion resistance depends on many parameters, but mainly on the grit size, grit velocity and impingement angle. The erosion parameters which were kept constant and those which varied from run to run, in order to characterize the erosion as completely as possible, are summarized in Table 1. The erosion performance was measured by weighing the samples before and after each test for different test durations, so that the evolution of the mass loss with time could also be determined. The erosion rate was expressed as the ratio between the volume loss and the grit mass sprayed on the sample.

Lastly, the effect of the coating on the Ti6Al4V base material was studied in terms of fatigue resistance. Using MFRC-ADAMEL equipment, coated Ti6Al4V cylinders were subjected to a sinusoidal force with a frequency of 50 Hz and a stress ratio equal to -1 (ratio between the minimum and maximum stress).

3. Results

3.1. Preliminary W or W–C single layers

The characterization results for the W and W–C, coatings obtained in our laboratory, have been described in detail elsewhere [8, 9]. Therefore, we will just focus here on the main characteristics that will help for the comprehension of the erosion test results.

The Vickers hardness of the coatings was measured as a function of the C content. The variation in the microhardness when increasing the C content is given in Fig. 1. The curve exhibits two maximum hardnesses of 26 000 MPa, the first for a C content of 14 at.%, the second for 40 at.%. The transition from the first peak to the second with increasing C content was found to correspond to a change in the crystallographic structure from the α-W structure to the β-WC_{1-x} non-stoichiometric structure.

Thus, if we examine the lattice dilatation of the α-W structure, derived from X-ray diffraction (XRD) patterns, with increasing C content from 0 to 22.5 at.% (Fig. 2), we can see that, up to 14 at.%, the lattice dilatation expands progressively and in the same proportion for all the main crystallographic directions, which explains the increase in microhardness, as observed by the curve in Fig. 1. Above 14 at.%, this expansion becomes anisotropic and the crystal lattice tends to collapse, which can be correlated with the drastic decrease in microhardness. In other words, the decrease in microhardness

TABLE 1. Erosion resistance test parameters

Fixed parameters		Variable parameters	
Grit nature	Angular silica	Grit flow rate	2 or 6 g min^{-1}
Air speed	240 m s^{-1}	Impact angle	30°–90°
Temperature	Room temperature	Average particle size	80–600 μm
Nozzle diameter	6 mm	Test duration	25 min (max)
Nozzle–sample distance	25 mm		

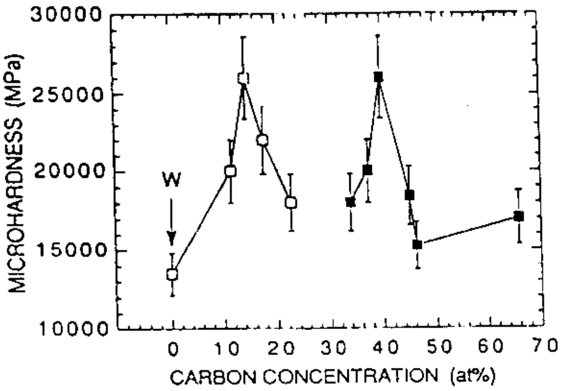

Fig. 1. Vickers hardness *vs.* C concentration in W–C coatings with the α-W structure (□) and the β-WC$_{1-x}$ structure (■). The indentation load was 50 gf.

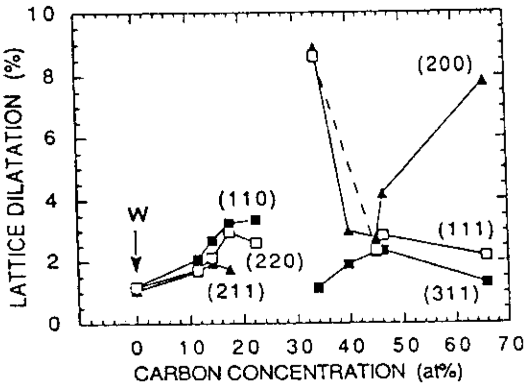

Fig. 2. Lattice dilatation *vs.* C concentration in W–C coatings. For C contents below 25 at.%, the lattice parameter of the α-W phase was calculated from the interplanar distance of (110) (■), (220) (□) and (211) (▲) planes. For C contents above 30at.%, the lattice parameter of the β-WC$_{1-x}$ phase was calculated from the interplanar distance of (200) (▲), (111) (□) and (311) (■) planes.

takes place when the material becomes anisotropic in terms of interplanar spacing or lattice dilatation.

A similar trend or behavior was observed for the C-rich coatings containing the WC$_{1-x}$ phase. The variation of the lattice dilatation with increasing C content (Fig. 2) shows that the maximum hardness at about 40 at.% C corresponds to the point where the lattice dilatation is the same for the three crystallographic directions considered. For the other C contents, the lattice dilatation is particularly anisotropic, corresponding to a low hardness.

3.2. Multilayers

Several coatings containing successive layers of W and W–C were deposited for erosion tests. Among the wide range of compositions offered by the PVD process, two compositions for the hard W–C layers—14 at.% and 40 at.% C—were chosen which correspond to the maximum hardness of 26 000 MPa. Two stacking arrangements were used, namely 6 and 12 layers for a total nominal thickness of about 60 μm. As a comparison, Mo/Mo–C and Cr/Cr–C multilayers were also prepared. The C contents considered for the Mo–C or Cr–C, *i.e.* 14 at.% and 18 at.% respectively, correspond to a solid solution phase in terms of crystallographic structure and a hardness of 24 000 MPa. The different samples tested are summarized in Table 2. The hardness values given in Table 2 and measured at a load of 1 kg are average values, because they integrate the effect of the ductile metal layers and hard metal–C layers. However, this is interesting information, as will be shown later.

The typical morphology of the W/W–C coatings is illustrated in Fig. 3, where a stacking arrangement composed of six layers is presented as an example. The photomicrograph shows a multilayer containing regularly deposited single layers forming a cohesive structure. Two kinds of layer are clearly visible, *i.e.* the W layers exhibiting a columnar microstructure and the W–C layers with a non-columnar, relatively dense microstructure.

The erosion performances of the different multilayers were first evaluated for two impingement angles of 45° and 90°. The multilayer coatings were compared with one another as well as with the base-line uncoated Ti6Al4V substrate and a TiN coating. The results are presented in Fig. 4. The erosion resistance is found to be dependent on the impingement angle with, in particular, the behavior of the W/W–C and TiN coatings comparable with those of brittle materials, since the erosion rate increases as the impingement angle increases. Furthermore, the W/WC$_{1-x}$ (5/5) coating exhibits very poor performance despite its very high hardness. This point will be discussed later.

TABLE 2. Characteristics of the coatings subjected to erosion tests at impingement angles of 45° and 90°

Coating[a]	Thickness (μm)	Number of layers	Nature of the hard layers	Surface hardness (MPa)
W/W–C(10/10)	54	6	Solid solution	21800
W/W–C(5/5)	61	12	Solid solution	20600
W/WC_{1-x}(10/10)	60	6	WC_{1-x} carbide	27600
W/WC_{1-x}(5/5)	61	12	WC_{1-x} carbide	32500
Mo/Mo–C(10/10)	52	6	Solid solution	14300
Mo/Mo–C(5/5)	52	12	Solid solution	14000
Cr/Cr–C(10/10)	60	6	Solid solution	11000
Cr/Cr–C(5/5)	58	12	Solid solution	10500
TiN	60	1	Nitride	18900

[a] The figures in parentheses indicate the nominal thicknesses of the single layers in micrometers.

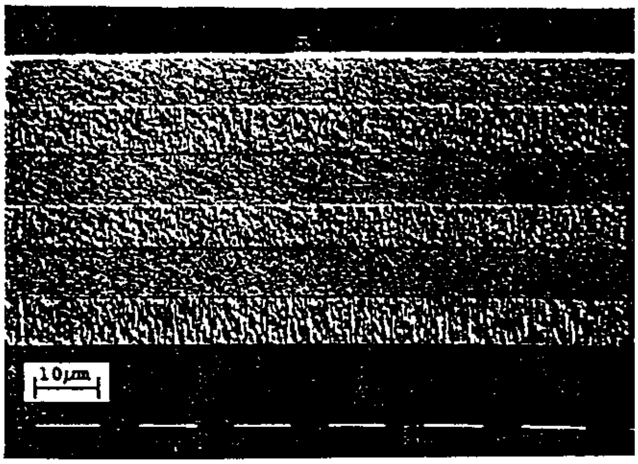

Fig. 3. Typical etched cross-section of a W/W–C (10/10) coating composed of six layers.

Among the different W/W–C multilayers, the W/W–C (5/5) clearly appears to be far superior to the others: practically, in our testing conditions and for a 90° impingement angle, only very little damage appeared before 25 min of testing, although, for the other multilayers, typically a period of 5 min was long enough to erode the whole coating. Compared with TiN, the erosion resistance provided by the W/W–C (5/5) coating is improved by factors of about 5 and 30 for impingement angles of 45° and 90° respectively. This erosion resistance is more than two orders of magnitude higher than the Ti alloy resistance.

Further characterizations were completed on the W/W–C (5/5) coating, as shown in Fig. 5, where the effect of the grit size was investigated for two impingement angles of 90° and 30°. For both angles, the erosion resistance of the W/W–C (5/5) coatings changes only slightly with the grit size. It must be pointed out that, even for a large grit size (600 μm), the resistance of the W/W–C (5/5) coatings remains particularly good. Moreover, this resistance remains unchanged after thermal treatment of the samples in air at 300 °C.

The eroded zone of each sample was examined by scanning electron microscopy (SEM). The scanning electron micrographs of the Mo/Mo–C and Cr/Cr–C samples show erosion craters with inclined side-walls, corresponding to progressive erosion of the coating. This behavior is confirmed by the fact that the erosion rate of these coatings is found to be independent of time. This result, typical of ductile materials, is in agreement with the low hardness found for these coatings. In contrast, the harder W/W–C coatings exhibit non-regular erosion and microcracks typical of brittle materials. Nevertheless, depending on the hard phase present

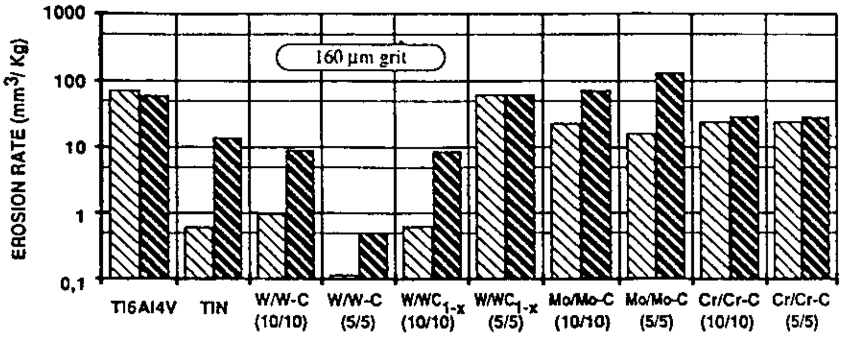

Fig. 4. Erosion resistance of the different coatings on Ti6Al4V alloy with average particle size of 160 μm, grit flow rate of 6 g min^{-1} and angles of particle impingement of 45° (▨) and 90° (▧).

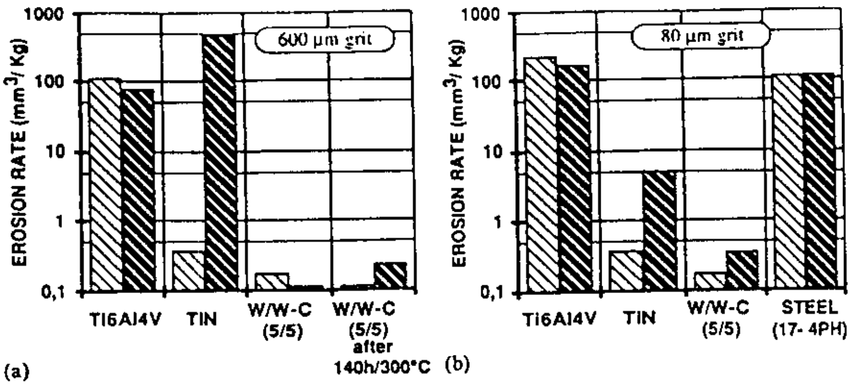

Fig. 5. Erosion resistance of W/W-C (5/5) coatings for grit size of (a) 600 µm and (b) 80 µm. The grit flow rate was 2 g min^{-1}. The angles of impingement were 30° (▨) and 90° (▨). TiN, Ti6Al4V and steel have also been tested.

in the multilayer, the propagation of microcracks through the coating seems different.

For the solid-solution-type W-C multilayers, microcracks propagating through the interface between W and W-C layers are observed. This crack deflection mechanism (Fig. 6(a)) improves the impact resistance until the rupture of the coating happens: the eroded zone shows sharp outlines (Fig. 6(b)). In contrast, the W/WC$_{1-x}$ multilayers containing a carbide phase show an eroded zone with different outlines, corresponding to steps originating in a gradual decohesion, layer by layer, of the coating (Fig. 6(c)). Moreover, the WC$_{1-x}$ layers are found to contain a lot of cracks which can be related to the very high brittleness of the layers, as was evidenced by indentation tests [9].

Lastly, different uncoated and W/W-C-coated Ti6Al4V specimens were tested by rotating bending tests. The Wöhler diagram (Fig. 7) shows that the coating has

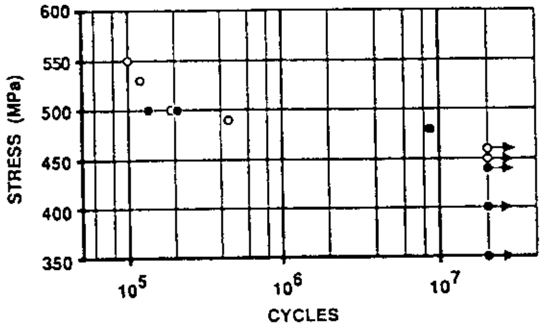

Fig. 7. High cycle fatigue performance of uncoated (○) and W/W-C (5/5)-coated (●) Ti6Al4V specimens. The coatings were deposited as W/W-C (5/5) samples with 12 layers 2 µm thick.

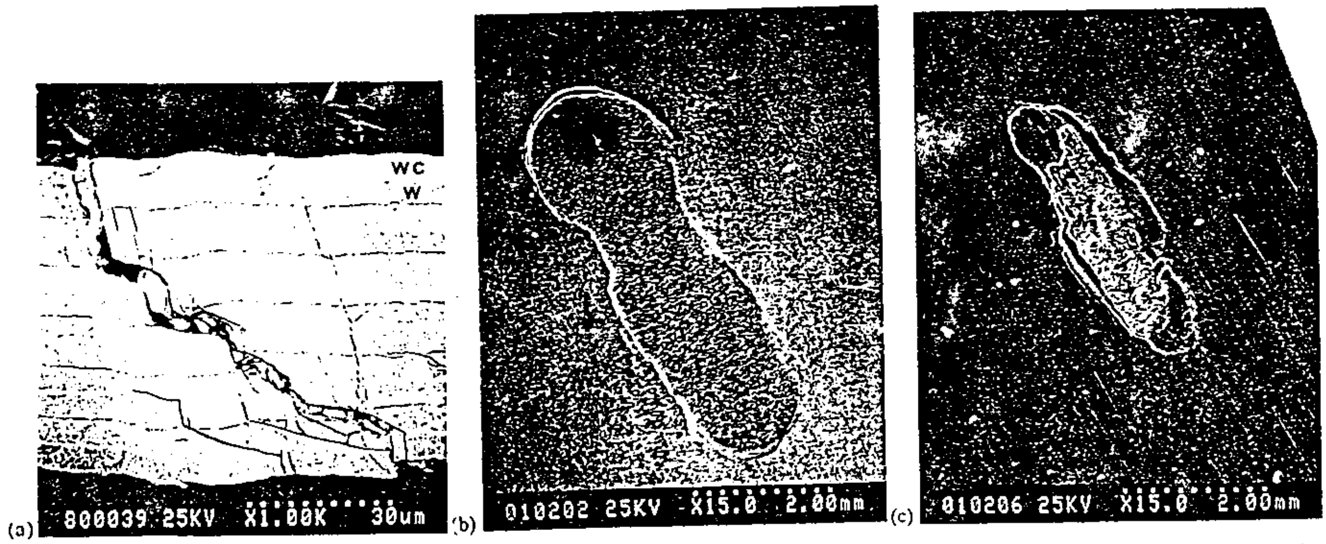

Fig. 6. SEM images (a) through the impact zone of a W/W-C (5/5) coating (exceptionally after 35 min of test), (b) of the eroded zone of a W/W-C (10/10) sample and (c) of the eroded zone of a W/WC$_{1-x}$ (10/10) sample.

no effect on the Ti6Al4V mechanical properties, which is in agreement with the compressive internal stresses measured in the coatings. Moreover, the fracture examination, after testing, showed that the failure grew from a machining defect on the substrate and was not related to the coating.

4. Discussion

The different results of erosion tests clearly show that the erosion resistance is closely related to the nature of the deposited coating, with a far superior behavior for the solid-solution-type W–C-based coating, on the whole. Nevertheless, the comparison with CVD WC multilayers reveals a quite different behavior to that of our PVD coatings [4].

It must be emphasized first that, compared with stainless steel, the improvement factor in erosion resistance can be estimated to be at least around 200 times (Fig. 5(b)) for the PVD W/W–C (5/5) coating, whereas it is only 3 times for CVD coatings. The fact that the erosion test conditions are different cannot explain such a performance gap. In addition, although for the CVD coatings the stacking arrangement does not appear as a predominant parameter, it is obvious that, in our case, this parameter is important. However, it depends on the W–C phase, since, for W/W–C solid solution multilayers, the higher the number of layers is, the better is the erosion resistance, whereas this is not the case for W/WC_{1-x} coatings.

This difference could be due to the difference in interface nature between the two kinds of multilayers, since, for the W/W–C solid solution coatings, there is a crystallographic continuity at the W–(W–C) interface which probably makes the bonding stronger, which is not the case for the $W–(WC_{1-x})$ interface. The fact that no decohesion cracks are found in W/W–C multilayers seems to support this idea.

These results suggest that two conditions must be fulfilled to produce multilayer coatings with a good erosion resistance: (i) the structure must contain very hard layers, able to resist, in particular, particle flux at small incident angles; (ii) the structure must exhibit strong interfacial cohesion between the different layers. If this is the case, it becomes possible to improve the erosion performance of the coating not only by increasing its thickness but also by changing the number and thickness of the single layers. As a result, the PVD process, by making possible the formation of a hard solid solution of W–C which has strong interfacial cohesion with pure W, constitutes a promising means for developing erosion-resistant coatings. However, a lot of investigations have still to be carried out to optimize the stacking arrangement.

5. Conclusions

This study has demonstrated that the deposition of W/W–C coatings can be accomplished by reactive magnetron sputtering which provides very highly erosion-resistant coatings. Compared with Ti-based alloys, the erosion resistance is at least improved by two orders of magnitude. This very good behavior seems related to the achievement by PVD of very hard W–C solid solution layers that can be closely combined with pure W layers. Finally, the mechanical properties of the substrate were found to be unaffected by the coating treatment.

Acknowledgments

This work has been supported by the French Ministry of Defense (Service Technique des Programmes Aéronautiques / Matériaux). The authors also wish to thank J. Ernoult for his expert technical assistance and sputter deposition work, M. Chaudet for electron microprobe analyses and scanning electron microscopy, and G. Coste for the erosion tests.

References

1 J. P. Massoud, Comportement à l'érosion par des particules solides d'un alliage de titane TA6V traité par laser, thèse de doctorat en génie des matériaux, INSA de Lyon.
2 P. N. Walsh and R. C. Tucker, Jr., *Surf. Coat. Technol.*, *54–55* (1992) 32.
3 V. Shanov, W. Tabakoff and M. Metwally, *Surf. Coat. Technol.*, *54–55* (1992) 25.
4 D. Garg and P. N. Dyer, in T. M. Besmann and B. M. Gallois (eds.), *Chemical Vapor Deposition of Refractory Metals and Ceramics, Mater. Res. Soc. Symp. Proc.*, *168* (1990) 213.
5 D. G. Bhat and R. A. Holzl, *Thin Solid Films*, *95* (1982) 105.
6 P. N. Dyer, D. Garg, S. Sunder, H. E. Hintermann and M. Maillat, *Proc. 12th Ann. Conf. on Composites and Advanced Ceramic Materials, Cocoa Beach, FL, January 17–22, 1988.*
7 A. Aubert, J. Danroc and J. P. Terrat, *Thin Solid Films*, *126* (1985) 61.
8 Y. Pauleau and Ph. Gouy-Pailler, *Mater. Lett.*, *13* (1992) 157.
9 Y. Pauleau and Ph. Gouy-Pailler, *J. Mater. Res.*, *7*(8) (1992) 2070.

Characterization of tungsten-carbon layers deposited on stainless steel by reactive magnetron sputtering

Y. Pauleau[a] and Ph. Gouy-Pailler
Centre d'Etudes Nucléaires de Grenoble, CEREM-DEM-SGS, 85X, 38041 Grenoble, France

(Received 30 October 1991; accepted 6 April 1992)

Tungsten-carbon coatings have been deposited on stainless steel substrates by reactive magnetron sputtering from Ar–CH_4 mixtures. The carbon concentration in the coatings measured by electron microprobe analyses was found to be proportional to the CH_4 flow rate. Only the cubic α–W phase with a dilated lattice parameter was identified in W–C coatings having a carbon content lower than 25 at. %. Since the lattice parameter of the α–W phase in these W–C coatings increased with increasing carbon content, these coatings may be assumed to be W–C solid solutions. Only the nonstoichiometric β-WC_{1-x} carbide (cubic phase) was detected in W–C coatings containing 30 to 70 at.% of carbon. The chemical state of the elements was investigated by x-ray photoelectron spectroscopy. The Vickers hardness of the W–C coatings was found to be considerably dependent on the carbon concentration. A maximum microhardness of 26 000 MPa was measured for W–C coatings containing either 14–15 at. % or 40–45 at. % of carbon. The correlation between crystallographic structure and microhardness is analyzed and discussed in this paper.

I. INTRODUCTION

Various physical or chemical vapor deposition methods have been investigated to produce tungsten carbide, tungsten-carbon alloys, or tungsten carbide with additive (cobalt) used as hard and protective coatings.[1] Relatively few attempts were directed toward the deposition of W–C coatings by reactive sputtering although this method was successfully applied to deposit a large variety of compounds with a wide range of properties difficult or impossible to obtain by other means.[2] Tungsten-carbon layers with a carbon concentration higher than 40 at. % have been reactively sputter deposited in an argon-acetylene plasma from either a W target using radio frequency (r.f.), as direct current (d.c.) magnetron sputtering systems,[3-10] or a WC target using r.f. diode sputtering equipment.[11] The structure, morphology, and mechanical properties (microhardness, friction coefficient, wear resistance) were investigated as functions of the substrate temperature.[3,7] A mixture of tungsten carbides, namely β-WC_{1-x} (cubic phase), α-W_2C (hexagonal phase), and W_3C (cubic phase) was obtained at a substrate temperature of 200 °C whereas, at higher temperatures, only the nonstoichiometric β-WC_{1-x} tungsten carbide was formed. Sputtered W–C layers with a carbon concentration varying from few at. % to about 40 at. % seem to be rather difficult to synthesize by using an Ar–C_2H_2 plasma; indeed, the amount of carbon in the deposited material was found to be about 46 at. % with a flow rate of acetylene injected in the sputtering chamber as low as 3 standard cm^3/min.[9] This difficulty may originate from the low stability of C_2H_2 and could be overcome by using a carbon precursor more stable than acetylene, namely methane, CH_4. Argon-methane mixtures containing less than 10 mol % of CH_4 were effective for reactive sputter deposition of W–C films from a W target.[12] The nonstoichiometric β-WC_{1-x} tungsten carbide was detected by x-ray diffraction analyses of these W–C films; however, the composition, structure, and properties of W-rich tungsten carbide films were not investigated in detail.

In this work, W–C coatings were deposited by reactive magnetron sputtering on stainless steel substrates using Ar–CH_4 gas mixtures. The carbon concentration in the material deposited with various CH_4 flow rates was determined by electron microprobe analyses. The structure, texture, and microhardness of the W–C coatings were investigated as functions of the carbon content. A correlation between the expansion of the lattice parameter and microhardness of the coatings was established.

II. EXPERIMENTAL PROCEDURE

The tungsten-carbon coatings were deposited on stainless steel (type 18/8) plates (2.5 × 2.5) cm^2 by the reactive d.c. magnetron sputtering method using a planar target of pure tungsten and argon-methane mixtures as a reactive gas. Prior to the deposition of coatings, the (2–3) mm thick stainless steel substrates polished by fine diamond paste were cleaned in trichlorethylene and al-

---

[a] Institut National Polytechnique de Grenoble, ENSEEG, B.P. 75, 38402 Saint Martin d'Hères, France.

cohol using an ultrasonic bath cleaner. The substrate was mounted on a substrate holder equipped with a chromel-alumel thermocouple for temperature measurements of the substrate during the deposition step. The substrates were not intentionally heated during sputter deposition of coatings. The sputtering chamber was evacuated by a pumping unit composed of a liquid nitrogen trap and an oil diffusion pump backed up with a mechanical pump; the base pressure was about 9×10^{-6} mbar. Pure argon and Ar–CH_4 mixtures were used as sputtering gases. The flow rate of the gases was measured and controlled by mass flowmeters. A shutter was placed in front of the W target to avoid any deposition and contamination on the substrate surface during the presputtering step and cleaning-up operation of the target. Prior to the deposition step, the substrate was polarized at −100 V and was ion etched for a few minutes; the temperature of the substrates rose up to 150 °C during this surface cleaning treatment. Then, the shutter was removed for the sputter deposition of coatings, and the substrate temperature reached about 250 °C in a few minutes. The maximum thickness of W–C coatings was in the range of 3.5 to 5 μm.

The carbon concentration in W–C thin films (0.5 to 1 μm in thickness) sputter-deposited on Si substrates was measured by nuclear reaction analyses [^{12}C(d,p)^{13}C] with an accuracy of about 1 at.%. Thicker W–C films were deposited on stainless steel substrates under similar sputtering conditions and were utilized as calibration samples for electron microprobe analyses (EMPA) of W–C coatings using a CAMEBAX instrument. The crystallographic structure of sputtered coatings was determined by x-ray diffraction (XRD) technique. The XRD patterns were obtained using a Co anticathode as an x-ray source. The chemical state of the elements in the W–C coatings was investigated by x-ray photoelectron spectroscopy (XPS). Photoelectron spectra were recorded using nonmonochromatized Mg K_α (1253.6 eV) radiation with a composite line width of 0.75 eV. Calibration in binding energy was performed by referencing the sample spectrum to the $Ag_{3d5/2}$ peak at 368.3 eV.[13]

III. RESULTS

The sputtered coatings, 3.5 to 5 μm in thickness, were tightly adherent to the stainless steel substrates. Tungsten-carbon coatings with a carbon content as low as 10 at.% were deposited with an excellent reproducibility by close control of the CH_4 flow rate. The carbon and tungsten concentrations in the deposited material measured by electron microprobe analyses were investigated as functions of the CH_4 flow rate. The W concentration decreased linearly and, correlatively, the carbon concentration increased linearly with increasing CH_4 flow rate. A similar variation in carbon content with the CH_4 content of the atmosphere was mentioned by Machida *et al.*[12] for W–C films produced by r.f. diode sputtering and analyzed by Auger electron spectroscopy.

The XRD data of sputtered W and W–C coatings containing less than 25 at.% of carbon are reported in Table I and typical XRD patterns are given in Fig. 1. Diffraction peaks observed in the XRD pattern of sputtered W coatings correspond to those of the cubic α–W phase; however, the relative peak intensities are different from those given in the JCPDS card.[14] The sputtered W coatings were preferentially oriented in the (111) direction. In addition, the position of the diffraction peaks is slightly shifted toward the low values of the diffraction angle (2θ); the corresponding dilatation of the crystal lattice resulting probably from mechanical stresses in the sputtered W coatings was about 1.1% (Fig. 2).

The XRD patterns of carbon-containing coatings exhibit diffraction peaks at diffraction angles (2θ) corresponding to those of W metal, and the interplanar distances, d, calculated from the XRD measurements match correctly with those of the cubic α–W phase reported in the JCPDS card[14] (Table I). A slight translation of the diffraction peaks toward low diffraction

TABLE I. Interplanar distances (d in Å) and peak intensities (I) of sputtered W and W–C coatings containing less than 25 at.% of carbon.

	W metal JCPDS data		Sputtered W		W–C 11.5 at.% C		W–C 14.3 at.% C		W–C 17.6 at.% C		W–C 22.5 at.% C	
hkl	*d*	*I*	*d*	*I*	*d*	*I*	*d*	*I*	*d*	*I*	*d*	*I*
110	2.238	100	2.265	100	2.285	100	2.298	100	2.311	100	2.313	100
200	1.582	15	1.589	0.7	1.609	1.7	...	...	...	...	...	...
211	1.292	23	1.305	13.5	1.313	8.4	1.317	5.4	1.315	4	1.268	3.5
220	1.119	8	1.132	12.9	1.138	13.5	1.143	14.8	1.152	9.3	1.148	12.3
310	1.001	11	...	...	1.017	4.3	...	...	...	...	...	...
222	0.914	4	0.923	52.3	0.925	14.9	...	...	...	...	...	...
321	0.846	18	...	...	...	...	...	...	...	...	...	...
400	0.791	2	...	...	...	...	...	...	...	...	...	...

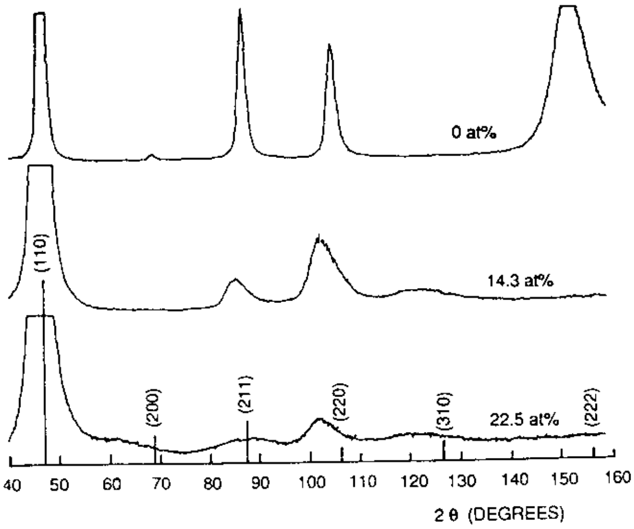

FIG. 1. Typical x-ray patterns of W and W–C coatings containing less than 25 at.% of carbon.

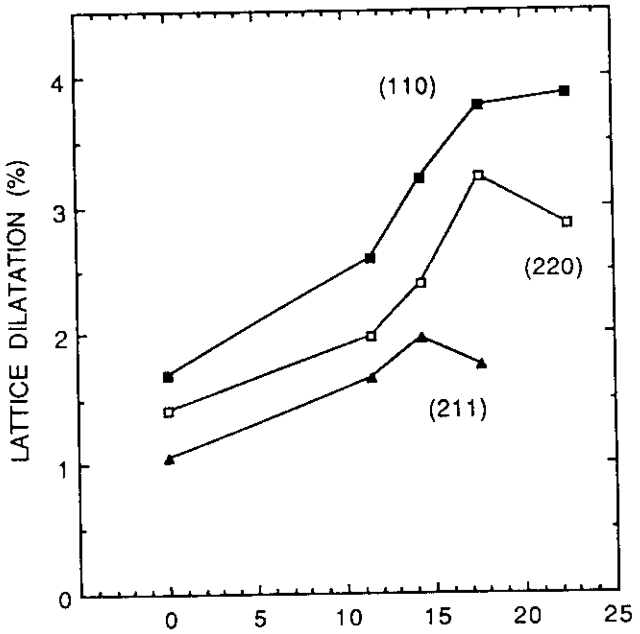

FIG. 2. Lattice dilatation of W–C coatings containing less than 25 at.% of carbon; the curves (220) and (110) are translated along the vertical axis by +0.25% and +0.50%, respectively.

angles (2θ) can be noticed as the carbon content in the W–C coatings increases. The interplanar spacings are found to be dependent on the carbon concentration in the coatings. As a result, the crystalline phase detected in the sputtered W–C coatings with a carbon content below 25 at.% may be assumed to be a solid solution of carbon in tungsten. In addition to the translation of the diffraction peaks, a broadening of the peaks and a decrease in peak intensities are observed as the carbon concentration in the coatings increases up to 22.5 at.% (Fig. 1). In other words, the expansion and deformation of the cubic lattice of W metal occur progressively with increasing carbon incorporation in the W–C coatings. The lattice parameter, a, was calculated on the basis of the diffraction angle corresponding to the (110), (220), and (211) lattice planes which provide the most intense peaks in the XRD patterns; then, the expansion of the crystal lattice, $(a-a_0)/a_0$, where a_0 is the lattice parameter of tungsten given in the JCPDS card[14] (a_0 = 3.1648 Å), was determined and plotted versus carbon concentration in Fig. 2 (for clarity, the curves corresponding to (220) and (110) lattice planes in Fig. 2 were translated along the vertical axis by +0.25% and +0.50%, respectively). A progressive and regular increase in the lattice parameter of the α–W phase can be observed up to a carbon content of about 15 at.%. For W–C coatings containing more than 15 at.% of carbon, the lattice dilatation depends on the crystal direction or family of lattice planes considered in the calculation of the lattice parameter. The interplanar distance in the (110) plane family increases continuously with increasing carbon content in the coatings; the maximum value of the lattice dilatation (and interplanar spacing) is equal to about 3.4% in W–C coatings containing 22.5 at.% of carbon. For the (220) planes, the lattice dilatation, i.e., the interplanar spacing, decreases as the carbon content in the coatings is greater than 18 at.%. Furthermore, the (211) diffraction peak is not observed in the XRD pattern of W–C samples with a carbon concentration of 22.5 at.% (Fig. 1).

These results suggest that the deposited material is relatively isotropic when the total concentration of carbon in the coatings is less than 15 at.%. Beyond this carbon concentration, an anisotropic behavior of the deposited material is observed and the cubic lattice tends to progressively collapse. The increase in the lattice parameter likely originates from both incorporation of carbon atoms in the cubic lattice of tungsten and mechanical stresses in the coatings.

Typical XRD patterns of W–C coatings containing more than 30 at.% of carbon are reported in Fig. 3. The interplanar distances, d, calculated from the XRD measurements and peak intensities are compared with the JCPDS data[15] in Table II; the diffraction peaks can be ascribed to the nonstoichiometric WC_{1-x} phase. This polycrystalline phase is similar to that deposited at higher temperatures (400–500 °C) by r.f. reactive magnetron sputtering of a W target in Ar–C_2H_2 mixtures.[3] For W–C coatings with a carbon content lower than 40 at.%, only 3 or 4 diffraction peaks can be detected in the XRD pattern. Most of the diffraction peaks corresponding to the cubic WC_{1-x} phase appear in the XRD pattern of the W–C coatings containing 45 at.%

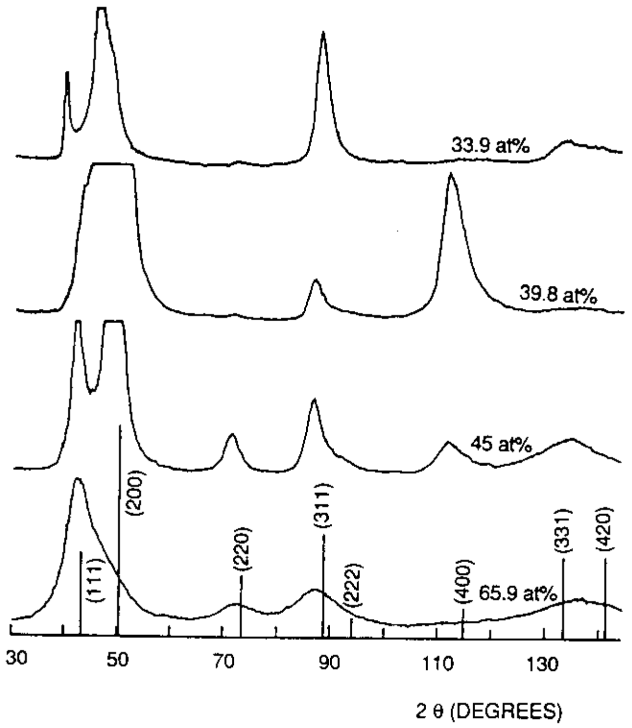

FIG. 3. Typical x-ray patterns of W–C coatings having a carbon concentration ranging from 30 to 70 at. %.

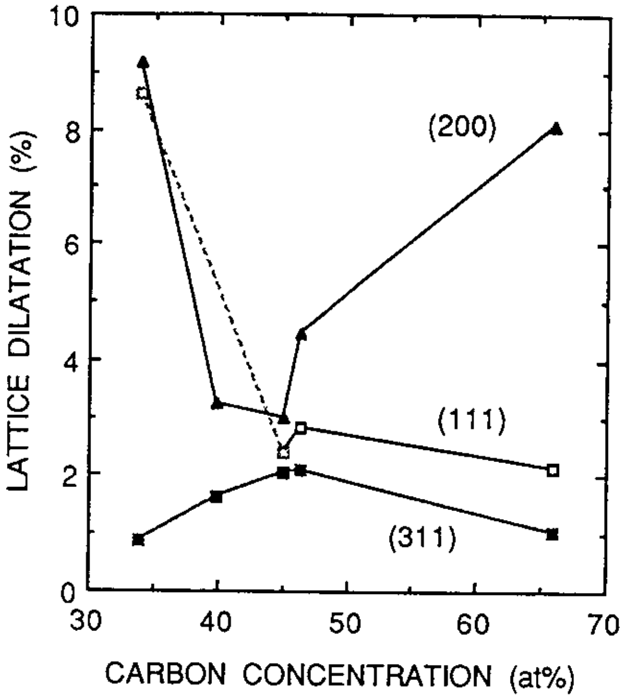

FIG. 4. Lattice dilatation of W–C coatings having a carbon concentration ranging from 30 to 70 at. %; the curves (200) and (311) are translated along the vertical axis by +0.25% and −0.25%, respectively.

of carbon. In addition, the relative peak intensities correspond approximately to those given in the JCPDS card. For W–C coatings containing more than 50 at. % of carbon, the diffraction peaks of the cubic WC_{1-x} phase broaden and the peak intensity ratio, $I_{(200)}/I_{(111)}$, is found to be reversed with respect to the ratio given in the JCPDS card; these (111) preferentially oriented coatings probably contained the saturated WC_{1-x} phase with $x = 0.33$ (or $WC_{0.66}$ containing 40 at. % of carbon according to the phase diagram of the W–C system[16]) and amorphous carbon in excess. The lattice dilatation of the WC_{1-x} phase was calculated from the diffraction angles corresponding to (200), (111), and (311) lattice planes which provide the most intense diffraction peaks. The variation in lattice parameter with respect to the value of the lattice parameter mentioned in the JCPDS card ($a_0 = 4.2355$ Å) depends on the carbon concentration in the coatings (Fig. 4). As already observed for the solid solution of carbon in tungsten, the lattice dilatation or the lattice parameter of the WC_{1-x} phase calculated from the XRD measurements can be significantly dependent on the family of lattice planes under consideration [for clarity, the curves corresponding to (200) and (311) planes in Fig. 4 were shifted along the vertical axis by +0.25% and −0.25%, respectively].

TABLE II. Interplanar distances (*d* in Å) and peak intensities (*I*) of sputtered W–C coatings containing more than 30 at. % of carbon.

	WC_{1-x} JCPDS data		W–C 33.9 at. % C		W–C 39.8 at. % C		W–C 45 at. % C		W–C 46.3 at. % C		W–C 65.9 at. % C	
hkl	*d*	*I*	*d*	*I*	*d*	*I*	*d*	*I*	*d*	*I*	*d*	*I*
111	2.429	40	2.639	14.2	2.401	7.6	2.487	33.7	2.498	82.6	2.482	100
200	2.107	100	2.294	100	2.170	100	2.165	100	2.195	100	2.272	51.9
220	1.495	30	...	...	...	...	1.532	10.1	1.521	35.2	1.516	17.7
311	1.277	50	1.291	60.8	1.301	2.5	1.306	16.2	1.307	30.4	1.293	47.3
222	1.221	10	...	...	...	...	...	...	...	...	...	...
400	1.061	15	...	...	1.077	13.6	1.080	13.2	...	...	...	...
331	0.973	40	0.974	27.7	...	...	0.973	26.9	0.971	80.5	...	...
420	0.948	40	...	...	...	...	...	...	...	...	...	...

For W–C coatings with a carbon content lower or greater than 45 at.%, a large deviation in the lattice dilatation can be observed, depending upon the crystal direction. The maximum value of the interplanar spacing expansion can reach 8.5% for the (200) plane family in W–C coatings containing 33 or 65 at.% of carbon. The lattice dilatation in W–C coatings with 39.8 at.% of carbon was not calculated from the (111) planes since the (111) diffraction peaks could not be detected in the x-ray pattern (Fig. 3). The lattice dilatation is independent of the direction considered in the crystal lattice for W–C coatings containing about 45 at.% of carbon, i.e., for the carbon saturated WC_{1-x} phase.

The morphology of the fracture cross sections of sputtered W and W–C coatings was examined by scanning electron microscopy. The visual aspect of the surface cross sections or the texture of the coatings was found to be very dependent on the carbon concentration (Fig. 5). A columnar texture with nearly parallel ridges perpendicular to the substrate surface can be observed for the sputtered W coatings. This texture is a characteristic feature of W films produced by sputtering.[17] The W–C

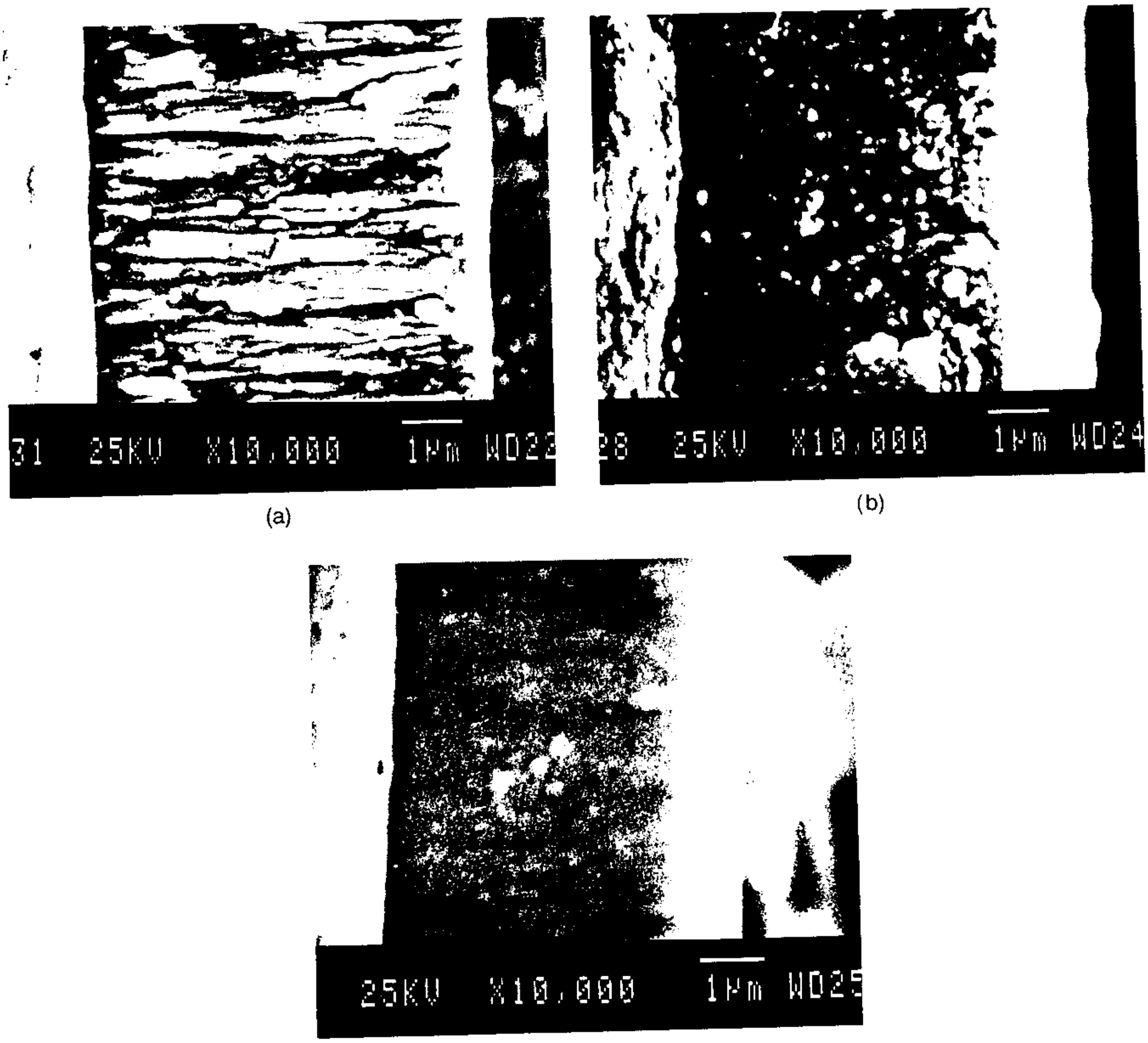

(a) (b)

(c)

FIG. 5. SEM micrographs of fracture cross sections of (a) W coating, (b) W–C solid solution coating with 14.3 at.% of carbon, and (c) WC_{1-x} tungsten carbide coating with 39.8 at.% of carbon deposited on stainless steel substrates; the substrate is located on the left side of the micrographs.

coatings with a carbon content of 14.3 at.% exhibit a nodular microstructure relatively dense with respect to the columnar structure of the W coatings. A finer and more uniform texture is observed for W–C coatings containing 39.8 at.% of carbon with a crystallographic structure corresponding to the WC_{1-x} phase.

The W–C coatings were analyzed by x-ray photoelectron spectroscopy after surface cleaning treatments of samples by argon ion etching. Typical XPS spectra of carbon in the W–C solid solution and WC_{1-x} phase are given in Fig. 6. After deconvolution of the C_{1s} peak, two binding energy peaks are observed at 285.1 eV and 283.4 eV both in W–C solid solution and WC_{1-x} phase. The position of the carbide species does not correspond to stoichiometric WC at 282.7 eV[18] but is typical of WC_{1-x} or W_2C.[6] The XPS spectra of $W_{4f7/2}$ of tungsten in these W–C coatings are exhibited in Fig. 7. The binding energy is observed at 31.5 eV and 31.9 eV in the W–C solid solution and WC_{1-x} phase, respectively. The results of semiquantitative XPS analyses of W–C coatings composed of the W–C solid solution or WC_{1-x} phase are summarized in Table III. The O atoms combined with W result from contamination of samples exposed to air. The oxygen contaminants were not fully eliminated from the surface after 45 min of ion etching since the surface of the W–C coatings was relatively rough and shadowing effects can occur during ion etching. The amount of C atoms combined with tungsten increases with increasing total amount of carbon measured by electron microprobe analyses of the coatings.

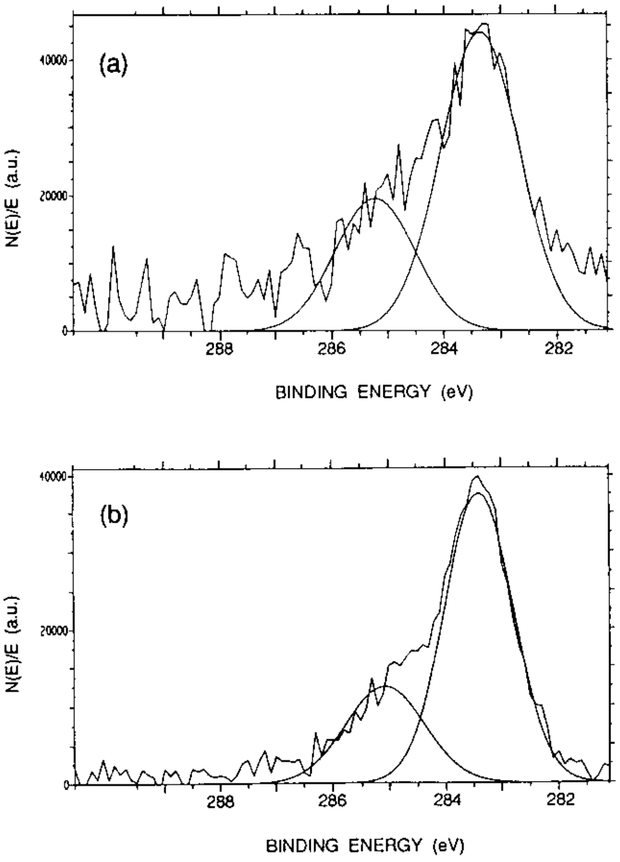

FIG. 6. XPS spectra of carbon (C_{1s} peak): (a) W–C solid solution, (b) WC_{1-x} tungsten carbide.

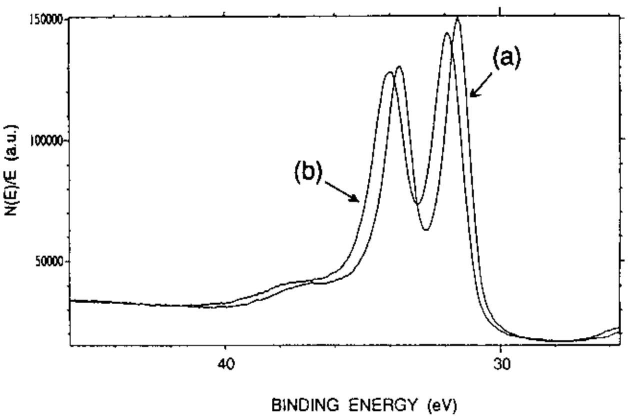

FIG. 7. XPS spectra of tungsten ($W_{4f7/2}$ peak) in W–C coatings. Curve (a): W–C solid solution coating; curve (b): WC_{1-x} tungsten carbide coating.

The Vickers microhardness of 4 to 5 μm thick W–C coatings measured under a load of 50 g was found dependent on the carbon concentration and crystallographic structure of coatings. The microhardness of sputtered W coatings is about 13 000 MPa (Fig. 8). The carbon incorporation in the crystal lattice of W leads to an increase in microhardness up to 26 000 MPa for a total carbon concentration of about 14 at.% in the W–C coatings. For higher carbon concentrations, the microhardness of W–C solid solution coatings decreases with increasing carbon content. The microhardness of WC_{1-x} coatings is plotted versus carbon concentration in Fig. 9. The hardness value increases with increasing carbon concentration; the maximum value is about 26 000 MPa, i.e., close to the maximum hardness of the W–C solid solution. The carbon concentration corresponding to a maximum hardness of the WC_{1-x} phase lies between 40 and 45 at.%. For carbon-rich tungsten carbide coatings with a carbon concentration of 45 to 65 at.%, the microhardness is stabilized in the range of 15 000 to 16 000 MPa. The variation in microhardness of sputtered W and W–C coatings with increasing load is given in Fig. 10. The microhardness of W coatings appears relatively independent of the load. The microhardness of W–C solid solution and tungsten carbide coatings increases rapidly with decreasing load (for clarity, the curves corresponding to the W–C coatings with 14.3 and 45 at.% of carbon were translated along the vertical axis by +5000 and +15 000 MPa, respectively). The microhardness of stainless steel substrates was about 6000 to 7000 MPa.

TABLE III. Semiquantitative XPS analyses of W–C coatings.

Structure XRD	Total carbon content (at. %) EPMA	Tungsten (at. %) W–C or W metal	W–O (WO_3)	W/C	Carbon (at. %) C–W	C–H	C–O	Total oxygen content (at. %)
Solid sol.	11.5	48.1	6.9	2.9	16.7	7.3	0	21
Solid sol.	22.5	49.4	5.6	1.8	27	5	0	13
WC_{1-x}	33.9	37.4	4.6	1.6	24	13.5	7.4	14
WC_{1-x}	39.8	34.6	4.4	0.9	36.5	14.5	0	10
WC_{1-x}	65.9	27	4	0.7	41.3	19.1	5.7	3

The variation of the microhardness with load shows that the values measured with a load of 50 g are characteristic of the coatings. The indentation patterns produced by the indenter with a load of 100 g are shown in Fig. 11. The pattern found in sputtered W coatings was very well defined. A slight deformation of the pattern with cracks at the rim can be observed for W–C solid solution coatings containing 22.5 at. % of carbon. More severe damage with delamination of the coating from the substrate can be noticed in the indentation pattern on tungsten carbide coatings with a carbon concentration of 39.8 at. %. The W–C coatings appear to become fragile and brittle as the carbon concentration in the coatings increases; however, a W–C coating with an α–W structure (or a W–C solid solution) seems to be more ductile than a W–C coating containing the WC_{1-x} phase. Indentation patterns with similar features were observed for WC_{1-x} coatings deposited by reactive sputtering from Ar–C_2H_2 mixtures.[4] In addition, the microhardness of these WC_{1-x} coatings measured with a load of 50 g was less than 24 000 MPa[4,9] or equal to 26 000 MPa[10] and was found to decrease with increasing carbon content in the coatings.[10]

IV. DISCUSSION

Tungsten-carbon coatings containing less than 20 at. % of carbon can be deposited by reactive magnetron sputtering using CH_4 as a carbon source. The carbon incorporation to the deposited material can be closely controlled to form either W–C solid solutions or a nonstoichiometric WC_{1-x} phase. The total amount of carbon incorporated in the W–C coatings was always found greater than the maximum solubility limit of carbon in the crystal lattice of tungsten; according to

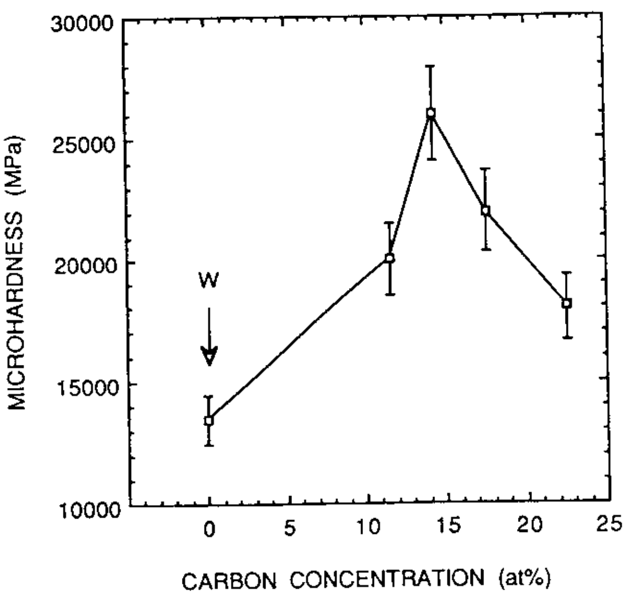

FIG. 8. Vickers hardness of W–C solid solution coatings under a load of 50 g.

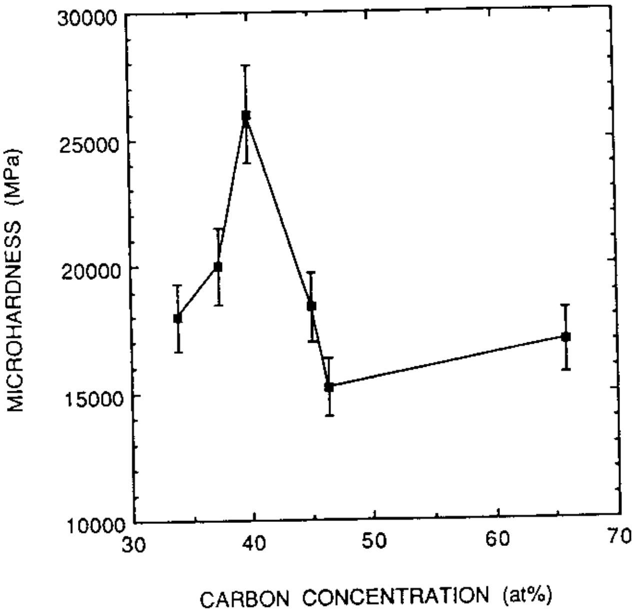

FIG. 9. Vickers hardness of WC_{1-x} tungsten carbide coatings under a load of 50 g.

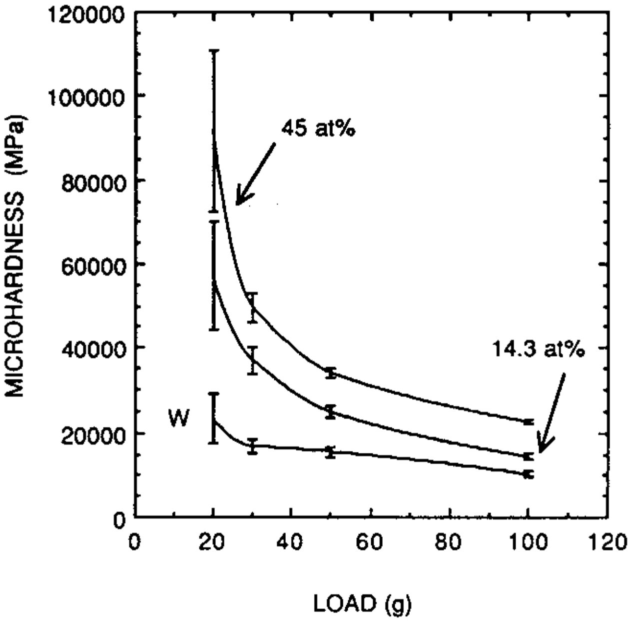

FIG. 10. Vickers hardness versus load of W and W–C coatings containing 14.3 at.% and 45 at.% of carbon; the curves 14.3 at.% and 45 at.% are translated along the vertical axis by +5000 and +15 000 MPa, respectively.

the equilibrium phase diagram of the W–C system, this maximum limit is about 1 at.% at 2700 °C.[16] The chemical state of carbon and tungsten atoms in these W–C coatings can be discussed on the basis of the XPS measurements by determining the chemical shift in the binding energy of a given core level electron of the element. The binding energy of 285.1 eV corresponds to the standard data given for C_{1s} peak in hydrocarbon compounds, labeled $(CH_2)_n$ (Fig. 6). The binding energy of 283.4 eV (Fig. 6) is in good agreement with the value of 283.4 eV reported by Srivastava *et al.*[6] and the value of 283.2 eV measured by Cavaleiro *et al.*[19] for nonstoichiometric carbide, WC_{1-x}; however, stoichiometric carbide, WC, typically has a C_{1s} binding energy of about 282.7 eV.[18] In fact, the binding energy measurements performed on W–C coatings deposited by sputtering lead to values lying between 284.5 eV and 282.8 eV which are the values of the binding energy corresponding to C_{1s} peak in pure graphite and in tungsten carbide, respectively.[13,20] The C_{1s} peak (Fig. 6) shows that two types of carbon atoms are always present in the coatings independently of the total concentration of carbon and crystallographic structure of the coatings. Carbon atoms identified as C_{1s} contaminant (binding energy at 285.1 eV) were detected on as-deposited samples as well as on samples cleaned by argon ion etching. These carbon atoms originated likely from the W–C matrix and appeared continuously at the sample surface during surface treatment by ion etching. In other words, this type of C atoms is inherent to the W–C samples. The second binding energy peak corresponding to C_{1s} at 283.4 eV may be associated with C atoms combined with W in a solid solution or in the WC_{1-x} phase. Thus, from the XPS measurements, it was not possible to distinguish clearly carbon atoms (in substitutional or interstitial positions) in the crystal lattice of W, i.e., carbon atoms in a W–C solid solution from carbon atoms linked to W atoms in the WC_{1-x} phase or carbon atoms in excess as an amorphous phase juxtaposed to the W–C crystallized phase. The concentration of carbon incorporated in the crystal lattice of W could not be measured from the XPS data. Although the lattice expansion deduced from XRD data increased progressively with increasing total concentration of carbon in the coatings, it cannot be concluded that the concentration of carbon atoms combined with W in a solid solution increased in the same manner; this variation in lattice parameter can result from mechanical stresses in the coatings which would be dependent on the total amount of carbon incorporated in the deposited material. As a result, the existence of a so-called "supersaturated" solid solution could not be demonstrated. The chemical state of W atoms also was analyzed by XPS in the W–C solid solution and WC_{1-x} phase (Fig. 7). The value of 31.5 eV for the $W_{4f7/2}$ peak in the solid solution agrees with the experimental values reported in the literature for the WC_{1-x} phase[6,19] and is close to the binding energy of 31.32 eV given for the $W_{4f7/2}$ peak in tungsten metal.[13] On the other hand, the binding energy of 31.9 eV corresponding to the $W_{4f7/2}$ peak measured on the WC_{1-x} phase is close to the value of 31.7 eV reported for WC samples after surface cleaning by Ar ion sputtering.[20] As a result, a significant shift in binding energy of the $W_{4f7/2}$ peak was observed between W–C solid solutions and WC_{1-x} tungsten carbide.

An interesting correlation can be established between crystallographic structure and microhardness. For WC solid solution coatings, the microhardness was maximum for a total carbon concentration of about 14 at.%. In fact, the microhardness increased progressively with increasing total carbon concentration up to 14 at.%. In this carbon concentration range, the crystal lattice of W expanded progressively and the lattice dilatation was found to be independent of the crystal direction (Fig. 2). For carbon concentration higher than 14 at.%, the lattice expansion becomes different according to the family of lattice planes considered in the calculation of the lattice parameter. In other words, the material was not isotropic; the crystal lattice tends to collapse and the microhardness decreases considerably. A similar trend or behavior can be noticed for WC_{1-x} coatings. The microhardness of the WC_{1-x} phase was found to be maximum for a carbon concentration of about 40 to 45 at.%. In this

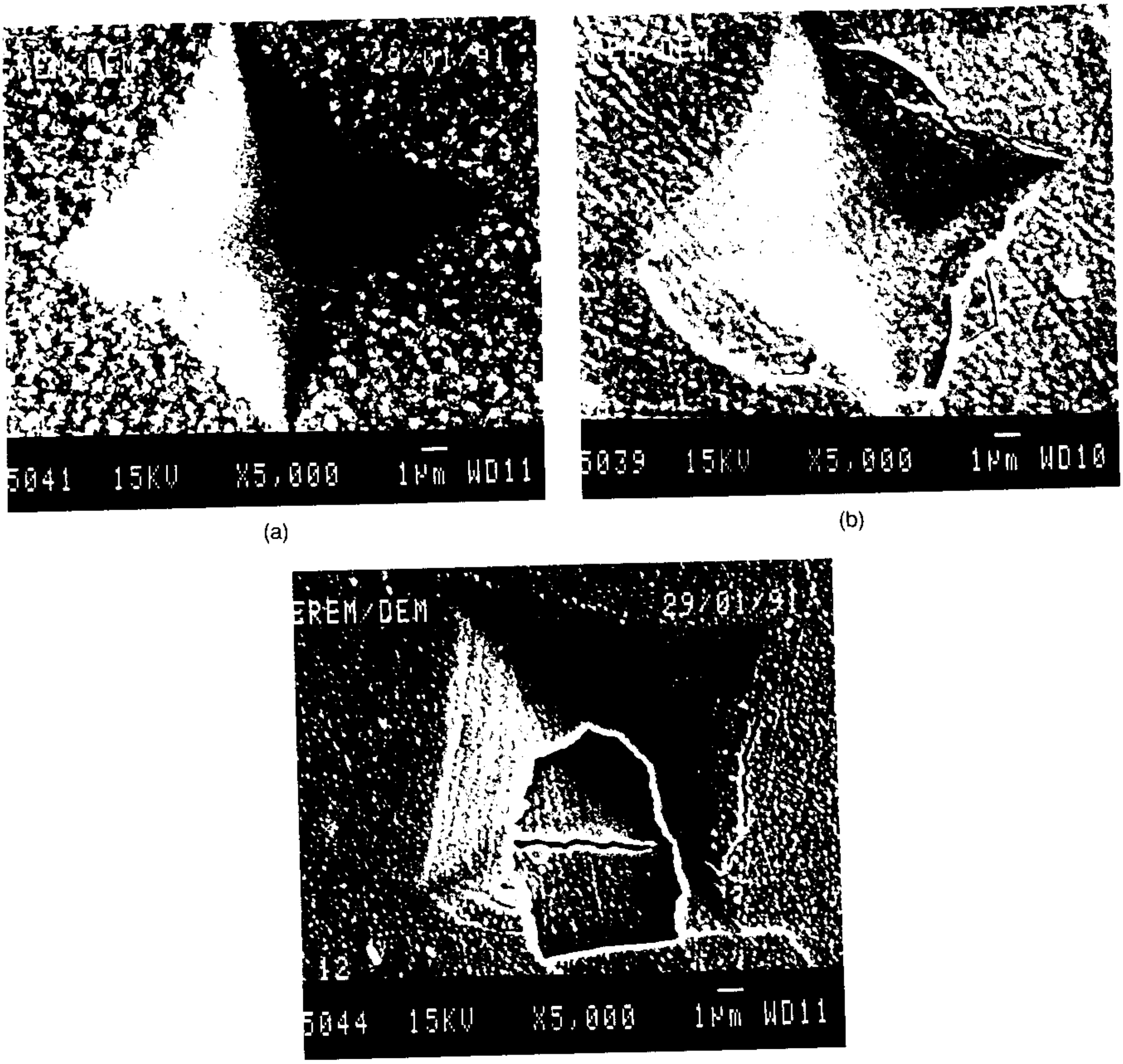

(a)

(b)

(c)

FIG. 11. SEM micrographs of indentation patterns under a load of 100 g in (a) W coating, (b) W–C solid solution coating with 22.5 at.% of carbon, and (c) WC_{1-x} tungsten carbide coating with 39.8 at.% of carbon.

range of carbon concentration, the lattice dilatation was independent of the crystal direction (Fig. 4). As a result, the microhardness of W–C coatings was maximum for isotropic materials in terms of interplanar spacing expansion or lattice dilatation.

V. CONCLUSION

This study has demonstrated that the deposition of W–C coatings can be accomplished by reactive magnetron sputtering with a close control of the carbon concentration (below 20 at.% of carbon) using CH_4 as a reactive gas. In these W–C coatings the α–W phase with an expanded lattice parameter was identified by XRD. Since the lattice dilatation increased with increasing carbon content, these W–C coatings may be assumed to be W–C solid solutions. The nonstoichiometric WC_{1-x} phase was detected in WC coatings having a carbon concentration in the range of 30 to 70 at.%. The chemical state of carbon examined by XPS analyses was found to be similar in W–C solid solutions and $W–C_{1-x}$ carbide phase; however, W–C solid solution and $W–C_{1-x}$ carbide phase are distinguishable on the basis of W_{4f} binding energies. The lattice expansion of these polycrystalline phases exhibited a maximum value at a carbon concentration equal to 14 at.% and about 40 at.% for the W–C solid solution and nonstoichiometric tungsten carbide, respectively. The maximum value of microhardness also was reached for W–C coatings containing 14 at.% and about 40 at.% of carbon. The structure of these coatings was isotropic in terms of dilatation of the lattice parameter. The lattice expansion can result from the carbon incorporation in the crystal lattice and mechanical stresses in the coatings.

ACKNOWLEDGMENTS

The authors wish to thank J. Ernoult for his expert technical assistance and sputter deposition work as well as M. Chaudet and J. Jolivet for electron microprobe analyses and scanning electron microscopy. We would also like to thank B. Bes and H. Dunlop from CRV for XPS analyses and fruitful discussions of the results.

REFERENCES

1. K. K. Yee, Intern. Met. Rev. **23** (1), 19 (1978).
2. W. D. Westwood, in *Handbook of Plasma Processing Technology: Fundamentals, Etching, Deposition, and Surface Interactions*, edited by S. M. Rossnagel, J. J. Cuomo, and W. D. Westwood (Noyes Data Corp., Park Ridge, NJ, 1989), p. 233.
3. P. K. Srivastava, T. V. Rao, V. D. Vankar, and K. L. Chopra, J. Vac. Sci. Technol. A **2** (3), 1261 (1984).
4. P. K. Srivastava, V. D. Vankar, and K. L. Chopra, J. Vac. Sci. Technol. A **3** (6), 2129 (1985).
5. P. K. Srivastava, V. D. Vankar, and K. L. Chopra, Bull. Mater. Sci. **8** (3), 379 (1986).
6. P. K. Srivastava, V. D. Vankar, and K. L. Chopra, J. Vac. Sci. Technol. A **4**, (6), 2819 (1986).
7. P. K. Srivastava, V. D. Vankar, and K. L. Chopra, Thin Solid Films **161**, 107 (1988).
8. K. Fuchs, P. Rödhammer, A. Tschulik, K. Kailer, R. Weirather, E. Bertel, and F. P. Netzer, 11th International Plansee Seminar **C11**, 207 (1985).
9. K. Fuchs, P. Rödhammer, E. Bertel, F. P. Netzer, and E. Gornik, Le Vide, Les Couches Minces **235** (suppl.), Vol. 2, 587 (1987).
10. W. van Duyn and B. van Lochem, Thin Solid Films **181**, 497 (1989).
11. C. E. Wickersham, E. L. Foster, and G. H. Stickford, J. Vac. Sci. Technol. **18** (2), 223 (1981).
12. K. Machida, M. Enyo, and I. Toyoshima, Thin Solid Films **161**, L91 (1988).
13. C. D. Wagner, in *Practical Surface Analysis*, 2nd ed., Vol. 1 "Auger and X-ray Photoelectron Spectroscopy", edited by D. Briggs and M. P. Seah (J. Wiley & Sons, New York, 1990), p. 595.
14. JCPDS Data Cards, 4-806, International Center of Diffraction Data, Swarthmore, PA (1988).
15. JCPDS Data Cards, 20-1316, International Center of Diffraction Data, Swarthmore, PA (1988).
16. E. Rudy, S. T. Windisch, and J. R. Hoffman, in *Fundamentals of Refractory Compounds*, edited by H. H. Hausner and M. G. Bowman (Plenum Press, New York, 1968), p. 37.
17. A. M. Haghiri-Gosnet, F. R. Ladan, C. Mayeux, H. Launois, and M. C. Jancour, J. Vac. Sci. Technol. A **7** (4), 2663 (1989).
18. H. Dunlop, private communication.
19. A. Cavaleiro, M. T. Vieira, and G. Lempérière, Thin Solid Films **185**, 199 (1990).
20. R. J. Colton and J. W. Rabalais, Inorg. Chem. **15** (1), 236 (1976).

Synthesis, Characterization and Applications of :

I - WEAR-RESISTANT COATINGS

II - LOW FRICTION COATINGS

Y. Pauleau
National Polytechnic Institute
of Grenoble

INTRODUCTION

- **DEFINITION OF WEAR**

  * Manifested by a loss of surface material from one or both surfaces subjected to relative motion

- **RELATIVE MOTION**

  * Macroscopically observable

  * Small microscopic vibration - fretting

  Example : between a bolt or rivet head and the surface in systems subjected to severe vibrations

- **WEAR/FRICTION RELATIONSHIP**

  * Wear occurs at the surface contact which is also the seat of the friction mechanism

  * Wear and friction are not simply related one to the other

  - low friction does not necessarily mean low wear and vice versa
  - with a given combination of materials one sometimes meets situations where as time proceeds the wear rate increases and the friction decreases

MECHANISMS OF WEAR

1. ADHESIVE WEAR
2. ABRASIVE WEAR
3. FATIGUE WEAR
4. CORROSIVE WEAR
5. WEAR BY FRETTING
6. TYPES OF WEAR

1. ADHESIVE WEAR

- **Materials surface is never absolutely flat**

  * Contact between surface occurs at the tips of asperities which then deform under load

- **Asperity interactions**

  * May lead to metallic adhesion resulting from interdiffusion of metallic materials in sliding contact promoted by temperature rise

- **Nature of the adhesion between asperities**

  * Modified by surface films such as oxide films on metallic materials
  * As the translation motion occurs surface films are partially disrupted and adhesion will occur at a certain proportion of these contact zones
  * Adhesion between asperities will lead to the formation of wear particles or debris in sliding contact

2. ABRASIVE WEAR

- **Arise from the cutting action of hard surfaces rubbing on softer materials**

  Examples :

  * **1st type : when hard surface asperities act like cutting tools and remove particles from softer materials**

  * **2nd type : when loose debris of any kind (sand particles or wear particles created by the primary wear process) are trapped between sliding surfaces**

- **Methods of reducing abrasive wear**

  * **First type of abrasive wear :**

  - by ensuring high quality of surface finish of the mating surfaces

  - No longer a serious problem with modern production methods

  * **Second type of abrasive wear :**

  - More difficult to eliminate

  - Sealing and filtration can reduce the wear due to extraneous material

  - desirable to provide grooves or other such recesses on the surfaces of bearings which allow the debris to "escape" from the contact geometry

3. FATIGUE WEAR

- **Occur after a large number of loading cycles if materials loaded and unloaded cyclically exhibit fatigue failure**

  * Sliding contact

  - fatigue mechanism by interaction of asperities leading to failure of asperities

  * Rolling contact

  - fatigue mechanism of failure even more important
  - cracks produced by fatigue lead to the removal of relatively large pieces of metal giving the characteristic "pitting" failures

- **Methods of reducing wear**

  * Adhesive and abrasive wear :

  - virtually eliminated using a lubricant film separating surfaces

  * Fatigue wear :

  - fatigue-type failures not excluded even with lubricant film since the applied load is still transmitted to the solid surfaces
  - however, propensity to fatigue-type failures decreases as the oil film thickness increases

4. CORROSIVE WEAR

- **Arise from the surface reactions with environment to form contaminant films**

  * **Corrosive environments may enhance the abrasive action of wear debris**

  Example :

  - **aluminum metal is a relatively soft material whereas aluminum oxide wear debris act as a very hard abrasive agent**

- **Corrosive effects are not always entirely deleterious**

  * **Oxide films prevent metal to metal contact and greatly reduce the coefficient of friction**

- **Method of reducing wear**

  * **So-called E.P. (extreme pressure) additives to lubricating oil produced surface films (chlorides, sulfides) and provide protective surface layers**

5. WEAR BY FRETTING

- **Not really a separate mechanism but arises in rather special circumstances**

  * Fretting effects associated with the contact of surfaces subjected to oscillation motion of relatively small amplitude (only a few µm)

  Example : between surfaces in contact such as bolted components, and components located by friction such as flanges shrunk onto shafts

- **Such contacts can exhibit a form of adhesive wear**

  * The debris trapped between surfaces can cause a second stage of abrasive wear

  * This effect leads to the interesting combination of a reduction in friction, but an increase in wear

  \- increase in wear arises from the second stage abrasive effects

  \- reduction in friction occurs because oscillatory motion tends to produce rough spherical wear particles acting rather like a series of small balls separating the surfaces

- **Fretting occurs in a corrosive environment (air)**

  * Increased abrasive action of harder oxidized wear particles may occur → fretting corrosion

  Example : with steel in air - fretting effects often occur in machines during transit due to the vibrational shocks incurred

  Great care is usually taken to unload all critical contacts in the machine before its transit

6. TYPES OF WEAR

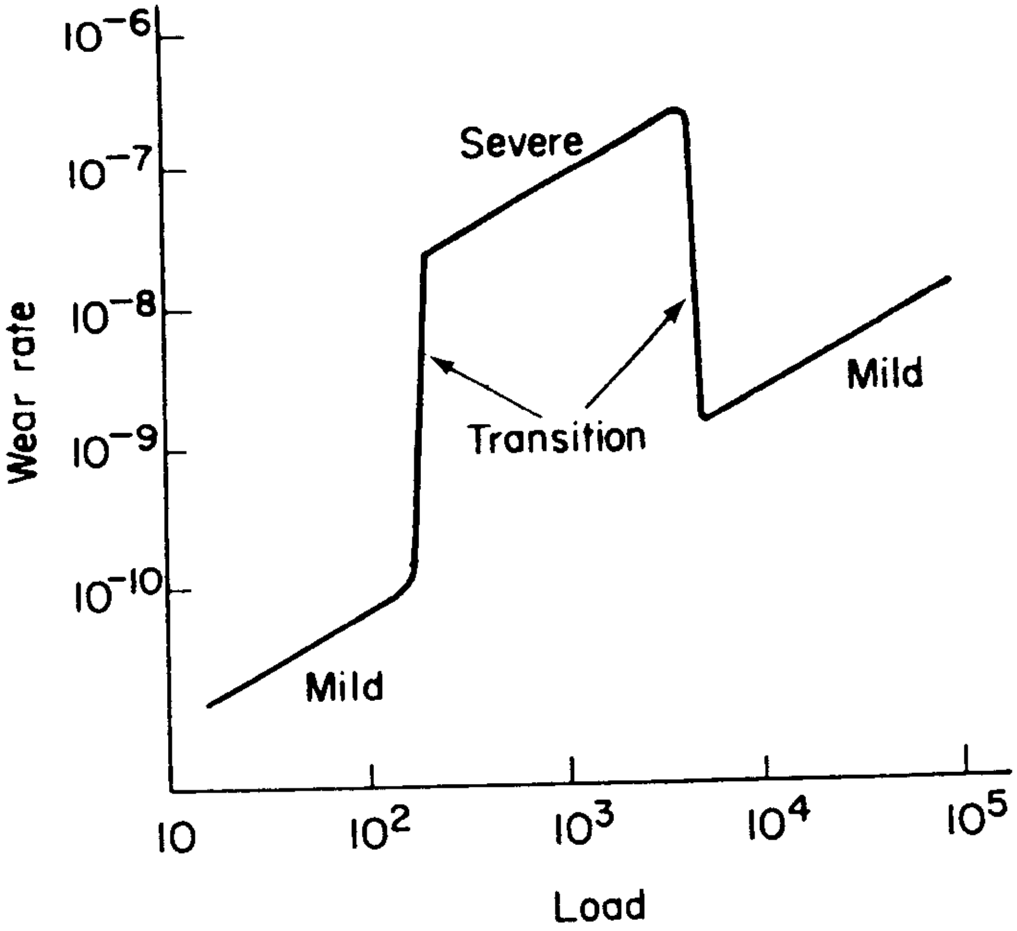

- **MILD WEAR**

  * Associated with low loads where metallic interactions are somewhat inhibited; thus, the wear debris consist of fine particles, usually oxide particles

- **SEVERE WEAR**

  * At higher loads where a much coarser wear process occurs

  * debris consist of a much larger particle-size

- **MILD WEAR AT HIGHER LOADS**

  * At higher loads, temperature rise in sliding contact cause metallurgical changes such as increase in materials hardness

WEAR/FRICTION TESTS

- **PIN-ON-DISK TRIBOLOGICAL TESTS**

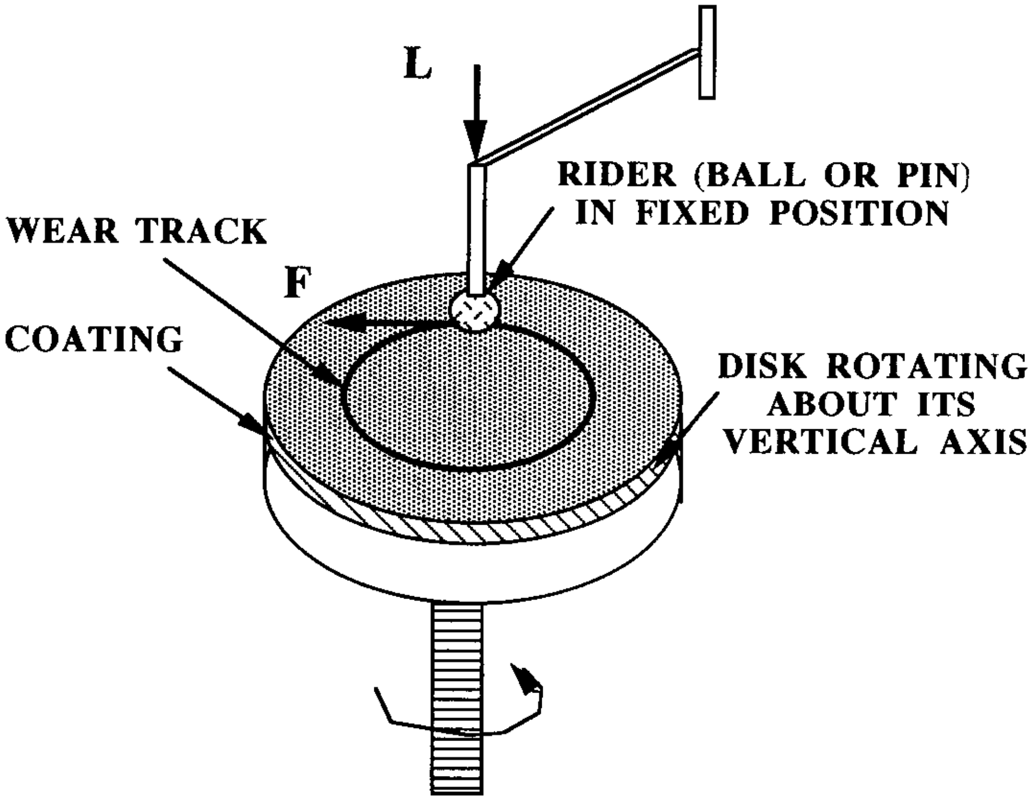

WEAR TESTS

- ## TYPICAL WEAR TESTING CONFIGURATIONS

Geometry	Motion	Geometry	Motion
	Unidirectional sliding		Reciprocating sliding
	Unidirectional or oscillatory sliding	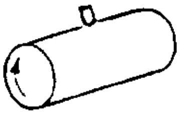	Unidirectional sliding
	Unidirectional sliding		Pure rolling and rolling plus sliding
	Unidirectional sliding		Small amplitude oscillatory sliding (fretting motion)
	Unidirectional sliding		Small amplitude oscillating sliding (fretting motion)
	Unidirectional sliding or unidirectional sliding plus oscillatory motion		Normal impact and normal impact plus sliding
	Unidirectional sliding		Normal impact
	Reciprocating sliding		

FACTORS AFFECTING WEAR BEHAVIOR

- HARDNESS
  - wear tends to be less the harder the material
- MUTUAL SOLUBILITY
  - wear is less where the mutual solubility is low
- CRYSTAL STRUCTURE
  - hexagonal close packed structure has the most limited deformation characteristics (it can only deform by slip along the basal plane)
  - h.c.p. gives good wear resistance - ex : Cobalt up to 417°C
- TEMPERATURE
  - operation temp. and/or temp. induced by friction phenomena
- CHEMICAL REACTIONS IN SLIDING CONTACT
  - interdiffusion phenomena, phase transformations and reactions with environment (tribochemistry)

Hard and wear-resistant coatings

- **HARDNESS, H (mean contact pressure)**

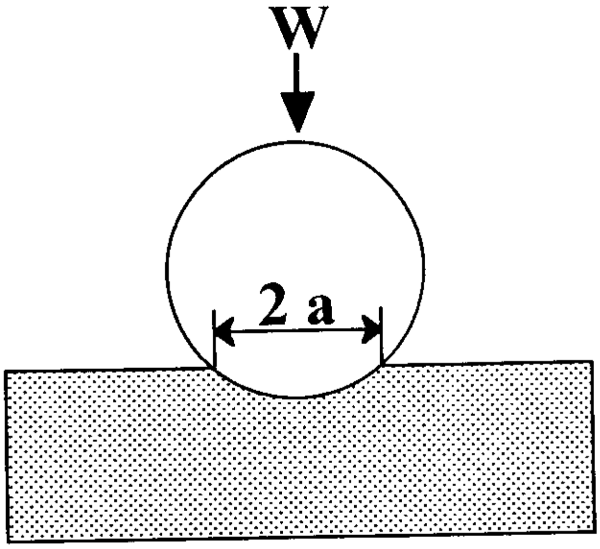

$$H = \frac{W}{A} = \frac{W}{\pi a^2}$$

○ **Permanent indentation pattern or (plastic indentation or deformation), when :**

$$H = 3\,\sigma_{0.2}$$

Volume of wear particles or debris

- **ADHESIVE WEAR**

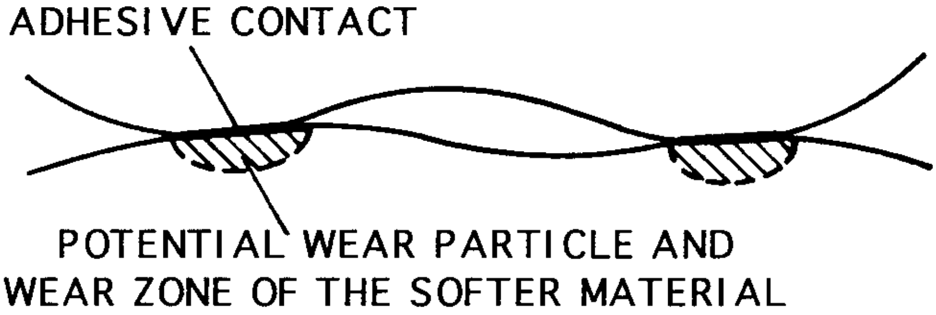

$\mathcal{A}$ **: REAL area of contact**

$$V = K\left(\mathcal{A} \times L\right)$$

○ **Archard relation :**

$$V = K\frac{W}{H}L$$

- **ABRASIVE WEAR**

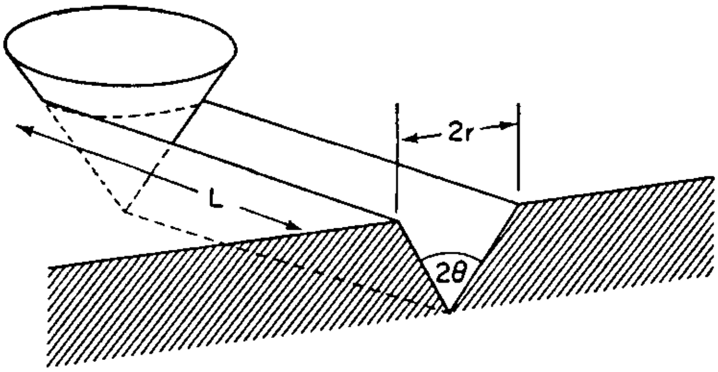

$$V = \frac{6\cot(\theta)}{\pi}\,\frac{W}{H}L = K_{ab}\,\frac{W}{H}L$$

Wear in sliding contact (dry friction)

- Example : non ferrous alloy/steel contact
- Severe wear with $H_{steel}/H_{alloy} > 1.5$
- Negligible wear with $H_{steel}/H_{alloy} > 0.4$
- Steel hardness for mechanical applications : $H_{steel} =$ 6 to 8 GPa
- Coating/non ferroux alloy : $H_{coating} =$ 15 to 20 GPa ----> negligible wear
- Coating of TiN, NbN, TiC, WC, ... on surfaces of two materials in sliding contact

HARD MATERIALS

- **HARDNESS DETERMINED BY :**
  - electronic and atomic structures - (intrinsic hardness)
  - microstructural features affecting the deformation mechanisms
- **HARD MATERIALS REQUIRE BOTH :**
  - high cohesive energy --> deep potential well
  - short bond length --> large curvature in the bottom of the well

INTRINSIC HARDNESS OF MATERIALS

- **DETERMINED BY :**
  - strength of the interactomic forces
  - crystal structure
- **MATERIALS WITH HIGH INTRINSIC HARDNESS :**
  - high cohesive energy
  - short bond length
  - high degree of covalent bonding

HARDNESS OF MATERIALS

- **Strength of interatomic forces and bond length determine the elastic properties of materials → HARDNESS**

  Example : **high elastic modulus implies :**

  - **large curvature of the atomic potential wells at the atom position corresponding to the minimum**

- **Intrinsically hard materials require :**
  - **high resistance to dislocation propagation and generation**
  - **low number of operative slip systems**

- **High resistance to dislocation propagation and generation (or multiplication) implies :**
  - **high bond strength**
  - **highly directional bonds such as covalent bonds**

    Example : **diamond (hardest material known) is completely covalent bonded material**

- **Many compounds have not purely covalent bonds → mixed character**
  - **hardness decreases as the proportion of covalent bonding decreases**

    Example : **TiC, TiN and TiO**

    - same crystal structure (B1-NaCl type) and similar lattice parameters

    - degree of covalent bonding decreases (and amount of ionic bonds increases) when the non metallic element is changed from C, to N, to O

    - hardness : 30, 20 and 10 GPa

PROPERTIES OF HARD TRANSITION METAL NITRIDES

- **Complex bonding structure**

  - characteristics of covalent, ionic and metallic bonds

- **Metallic character**

  - high thermal and electrical conductivities
  - metallic lustre

  Example : for TiN, VN and ZrN interband transitions cause reflectance edge located in the middle of the visible region → golden color

- **Covalent nature of bonds**

  - high microhardness : 20 to 30 GPa

HARD MATERIALS versus HARD COATINGS

- **HARD MATERIALS :**
  - suffer from low ductility
  - susceptible to brittle fracture
  - cannot be used in many applications with high intensities of load applied to sliding contact

- **IN SUCH CASES :**
  - more ductile bulk material coated with a hard wear-resistant coating is used

- **Hardness of materials surfaces can be improved by :**
  - SURFACE MODIFICATION TECHNIQUES
    - laser-induced surface hardening
    - ion implantation
    - carburizing or nitriding processes
  - DEPOSITION OF COATINGS VIA VARIOUS TECHNIQUES
    - plasma and flame spraying
    - electroplating
    - chemical vapor deposition (CVD)
    - physical vapor deposition (PVD)

Strengthening of polycrystalline materials

- Hard and wear-resistant coatings
- Improvement of mechanical properties of polycrystalline materials (interest in hard coatings)
- Hardening and improvement of mechanical properties of polycrystalline metallic materials : work hardening, boundary strengthening and solid-solution strengthening
- Mechanical properties of polycrystalline composite materials

Improvement of mechanical properties of polycrystalline materials

- Principle : reduce the dislocation motion within the material by introducing obstacles
- Grain boundaries - (work hardening)
- Solute atoms - (solid solution strengthening)
- Particles dispersed through out the metallic matrix - (dispersion-strengthened composites and particle-reinforced composites)

Improvement of mechanical properties of polycrystalline metallic materials

- SLIP PLANE CONTAINING AN ARRAY OF ***OBSTACLES***

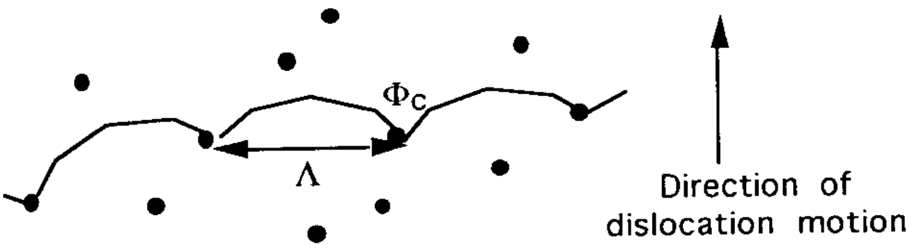

Λ : mean distance between obstacles

Φ_c : critical angle of curvature of dislocations (critical extrusion angle)

- **Maximum local stress, τ, to produce continued motion of the dislocation through the obstacle array :**

$$\tau \approx \frac{2\,T}{b\,\Lambda}$$

b : Burgers vector
T : line tension of the dislocation or line energy of the dislocation per unit length

$$T = \frac{G_m\,b^2}{2}$$

G_m : shear modulus of the matrix material

- **Maximum local stress, τ , or *Orowan stress* :**

$$\tau \approx \frac{G_m\,b}{\Lambda}$$

Strengthening of polycrystalline metallic materials

- INCREASE IN DENSITY OF *OBSTACLES*
- *Dislocation intersections*
- by cold deformation for work hardening of material
- *Grain boundaries*
- reduction in grain size
- *Dispersed particles or dispersed phase*
- elaboration of composite material

Strengthening by cold deformation

- **If each dislocation contains one dislocation intersection (obstacle) :**

$$\Lambda^2 \rho = \text{Constant}$$

ρ = Average density of dislocations

○ **Deformation stress for a cold deformed material, τ (or shear flow strength for a work hardened material) :**

- From the Orowan stress, $\tau = \frac{G_m b}{\Lambda}$, we can write :

$$\tau = \tau_0 + \alpha G b \sqrt{\rho}$$

τ_0 : Intrinsic flow strength of the material absent dislocations

α : Correction factor (necessitated by the approximate nature of the expression of τ)

$\alpha \approx 0.4$ (for body-centered cubic metals)
$\alpha = 0.2$ (for face-centered cubic metals)

Strengthening by grain boundaries

- Prior to macroscopic yielding, microscopic yielding can occur in a grain ① with slip systems oriented favorably with respect to the applied tensile force

  Dislocations within grain ① pile up against the grain boundary separating it from grain ② not so favorably oriented leading to :

  - high internal stress level within grain ① and
  - activation or initiation of slip in the nondeforming grain ②

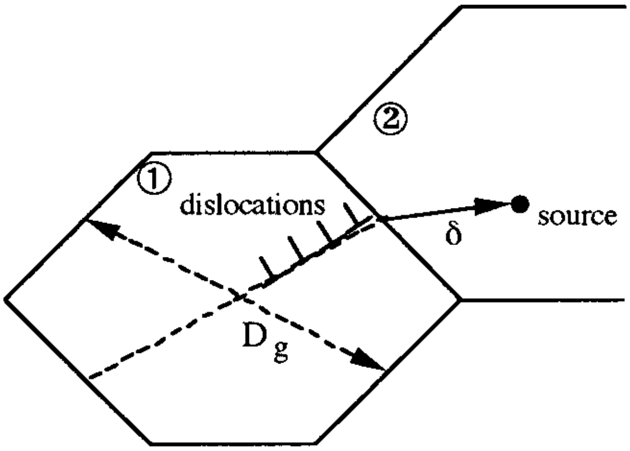

○ **Dislocation activation in grain ② occurs when :**

$$\tau^* = \left(\tau_{app} - \tau_0\right)\left(\frac{D_g}{4\,\delta}\right)^{1/2}$$

τ^* : Stress required for activation of dislocations in the unfavorably oriented grain ②

τ_{app} : Applied shear stress at which dislocation activation occurs in grain ②

τ_0 : Intrinsic stress resisting dislocation motion in the deforming grain ①

Strengthening by grain boundaries (continued)

- Shear stress, τ_{app}, required for deformation is dependent on the grain size, D_g :

$$\tau_{app} = \tau_0 + 2\,\tau^*\sqrt{\delta}\left(\frac{1}{D_g}\right)^{1/2}$$

$$\text{ou}\quad \tau_{app} = \tau_0 + k'\,\frac{1}{\sqrt{D_g}}$$

- Applied shear stress required for deformation of the material or tensile yield strength of the material :
  Hall-Petch relation

$$\sigma = \sigma_0 + k\,\frac{1}{\sqrt{D_g}}$$

Strengthening by grain boundaries
(continued)

- **Deformation effect**

1) **Plastic deformation** → increase in density of dislocations (dislocations pile up) or "statistically stored dislocations" corresponding to a density of dislocations ρ_S

2) **Internal deformation gradient** → formation and dislocations pile up or "geometrically necessary dislocations" of density ρ_G :

$$\rho_G \approx \frac{\bar{\varepsilon}}{b\,D_g} \qquad \bar{\varepsilon} = \text{ average shear plastic strain}$$

Thus : additional dislocation strengthening

○ With relatively small grain size → $\rho_G >> \rho_S$
and the flow stress is proportional to ρ_G :

$$\sigma = \sigma_0 + \left[k + \alpha\, G\, b \left(\frac{\bar{\varepsilon}}{b}\right)^{1/2}\right] \frac{1}{\sqrt{D_g}} \qquad \text{ou}$$

$$\sigma = \sigma_0 + k'' \frac{1}{\sqrt{D_g}}$$

○ **Remark** : k" increases as the shear strain $\bar{\varepsilon}$ increases
(observed experimentally at relatively low deformation strains)

Strengthening by cell boundaries or subboundaries

- **Other effects or other factors**

1) Grain boundaries markedly increase the strength of material for gain size < 5 µm

2) Formation of subboundaries → k'' approaches a constant, limiting value
and for larger deformation, subboundaries or cell boundaries may impede more effectively deformation motion than grain boudaries

○ Yield strength of material associated with cell boundaries :

$$\sigma = \sigma_0 + k''' \frac{1}{\sqrt{D'}}$$

D' : subboundary or cell boundary size

○ Remarks :

1) $k''' = 1/2$ to $1/5\ k$
thus : grain boundaries more effective barriers to dislocation motion than subboundaries (in principle)
HOWEVER, subboundary size, $D' < D_g$

2) sometimes, σ proportional to $1/D'$ rather than to $(1/D')^{1/2}$
(within experimental accuracy)
- logical result, assuming that : $D' \approx \Lambda$

Mechanical behavior of composite materials

① **<u>Dispersion-strengthened composites</u>**
(matrix = major component bearing the load)
d = 0.01 to 0.1 μm and f = 1 to 15 %

② **<u>Particle-reinforced composites</u>**
d > 1 μm and f > 25 %

③ **<u>Fibrous reinforcement in continuous-fiber composites</u>**
(fibers dispersed through out the composite)

- **Curvature and motion of dislocations in dispersion-strengthened composites (diameter of particles = d)**

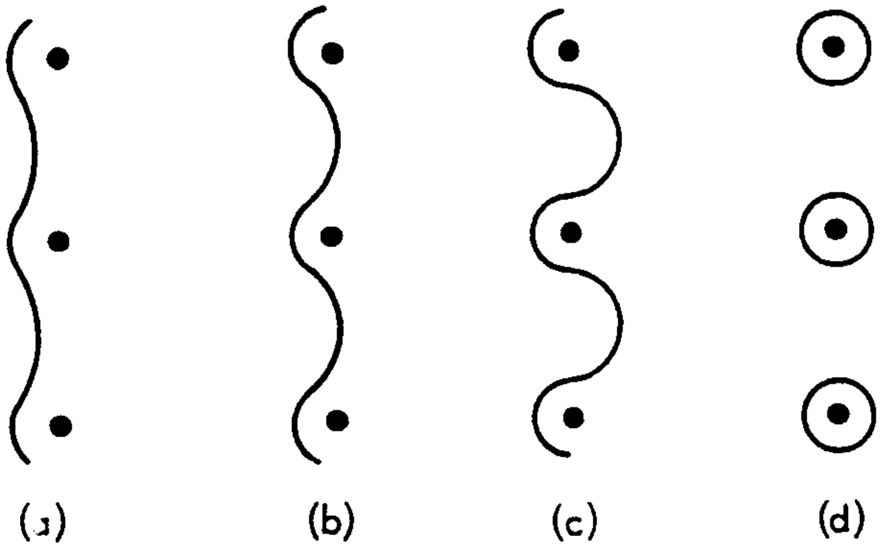

Mechanical behavior of composite materials (continued)

- **Calculation of Orowan stress <u>refined by Ashby</u>**

Other contributions to the critical shear stress :
- elastic strain in the matrix surrounding the particle
- difference in elastic constants between particle and matrix

$$\tau = \frac{1}{2\pi} \frac{G_m b}{\Lambda} \ln\left(\frac{d}{b}\right)$$

- **Macroscopic shear stress : $\sigma = 0.85\,\tau$**
  0.85 : "statistical factor" related to various values possible for particle spacing Λ and extrusion angle Φ_c; thus :

$$\sigma - \sigma_0 = 0.85\,\frac{G_m b}{2\pi\Lambda} \ln\left(\frac{d}{b}\right)$$

Avec $\Lambda = \frac{1}{\sqrt{N_P}}$

σ : Tensile yield stress applied to the composite material
σ_0 : Tensile yield stress applied to the pure matrix material
N_P : Number of particles intersecting a unit area of the slip plane

PROTECTIVE COATINGS PRODUCED BY ELECTRON BEAM PHYSICAL VAPOR DEPOSITION - (EB-PVD)

Y. PAULEAU
INP Grenoble

Objectives

- Substitute for electroplated hard chromium coatings - (hazardous for environment)
- Prepare thick protective coatings - (resistant against wear, corrosion, oxidation, …)

Attractive coatings and materials

- Multifunction coatings
- Composite coatings
- Multilayer coatings
- Functionally-graded coatings - (FGC)
- Ceramic materials (associated with a metallic matrix) - oxides (Al_2O_3, ZrO_2, SiO_2 ,...) - borides (TiB_2, ZrB_2, ...) - nitrides (TiN, Si_3N_4, AlN, CN, ...) - carbides (TiC, SiC, ZrC, HfC, AlC, ...)

Advantages of EB-PVD process

- High deposition rates
- Dense layers
- Control of composition (high purity)
- Columnar, polycrystalline, amorphous structures
- High thermal yield
- Low deposition temperatures even for ceramic and refractory materials
- Deposition of metallic/ceramic multilayer coatings on substrates with large surface areas
- No hazardous residue or reject (environment protection)

Ion-assisted deposition process

- *In situ ion etching of substrate surface*
- Improved adhesion
- Control of coating density and residual stresses

Fundamental aspects

- Mechanisms of vapor condensation and growth of coatings
- Interface phenomena and interactions (composite and multilayer coatings)
- Physical chemistry of evaporation process
- Correlations between : deposition parameters, physical characteristics of evaporation process and properties of coatings

EB-PVD equipment (ARL)

270 KW ELECTRON BEAM PVD PROCESS

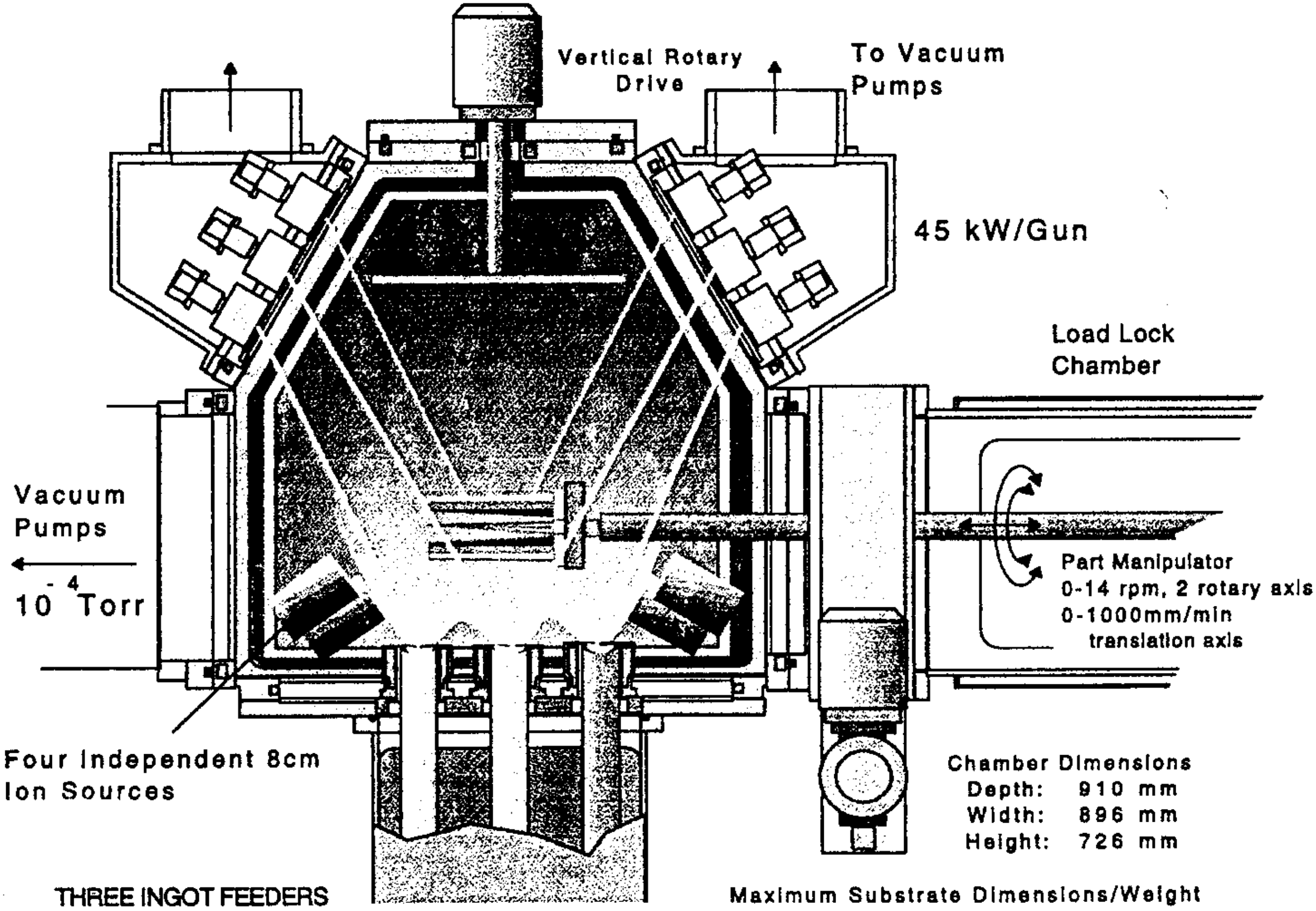

Chamber Dimensions
Depth: 910 mm
Width: 896 mm
Height: 726 mm

THREE INGOT FEEDERS
70mm diam. x 500mm long ingots
0.15 to 15 mm/min Feedrate

Maximum Substrate Dimensions/Weight
Horizontally Fed Cylinder:
200 diam. x 280 mm / 20kg
Vertically Held Disc: 400 mm diam. / 100 kg

Experimental procedure

Evaporation source

- Cylindrical ingots (rods)
  $\Phi = 50$ mm, length = 50 to 60 cm
  produced by cold pressing of powdery materials followed by sintering at 1800-2400°C in pure hydrogen

- electron beam
  intensity = 1 to 1.5 A
  accelerating voltage = 14 to 16 kV

Mo or Ta substrates

- (200 x 65) mm^2, thickness = 0.5 mm
- heated by electron beam between 600 and 1600°C

Pure TiC coatings

- direct evaporation of TiC rod

Ti-TiC multilayer coatings

- direct co-evaporation of Ti rod and TiC rod
- rotating substrates
- thickness control of elementary layers by adjusting deposition rate of materials and rotating speed of substrates

TiC coatings produced by direct evaporation

- **Cubic (NaCl type) structure and composition**

sample #	Vd (μm/min)	Ts (°C)	a (Å)	Preferred orientation	C/Ti ratio
TiC - A	0.41	700	4.321	111	0.65
		840	4.322	200	0.66
		1160	4.330	111	0.70
		1260	4.329	111	0.70
TiC - B	0.09	680	4.320	200	0.65
		860	4.320	200	0.65
		1200	4.320	200	0.65
		1340	4.320	200	0.65

- **Vickers hardness on the cross-section (and surface)**

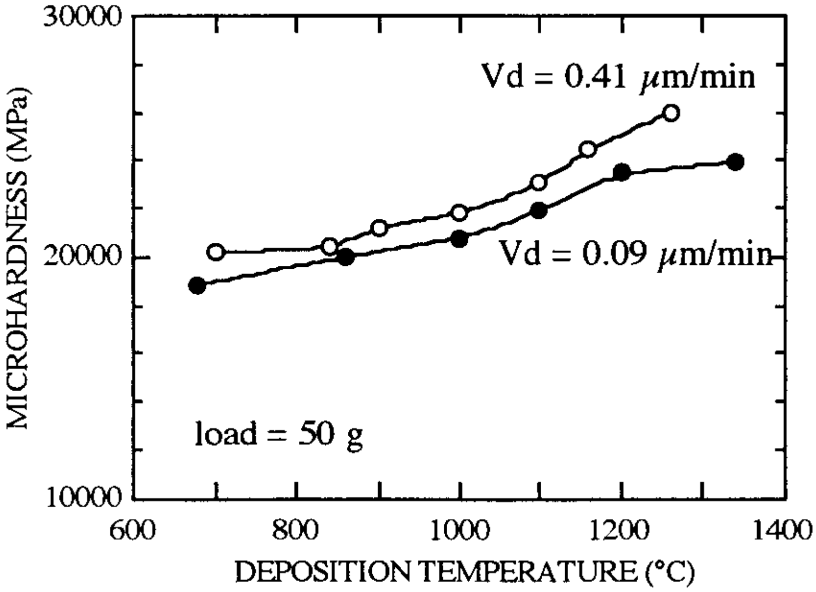

Ti-TiC multilayer coatings

Characteristics of samples

- thickness = 1 mm ; substrate : Mo ; T_s = 960°C ; V_d = 50 µm/min
- thickness of elementary layers : sample (a) 9 µm
  sample (b) 3 µm

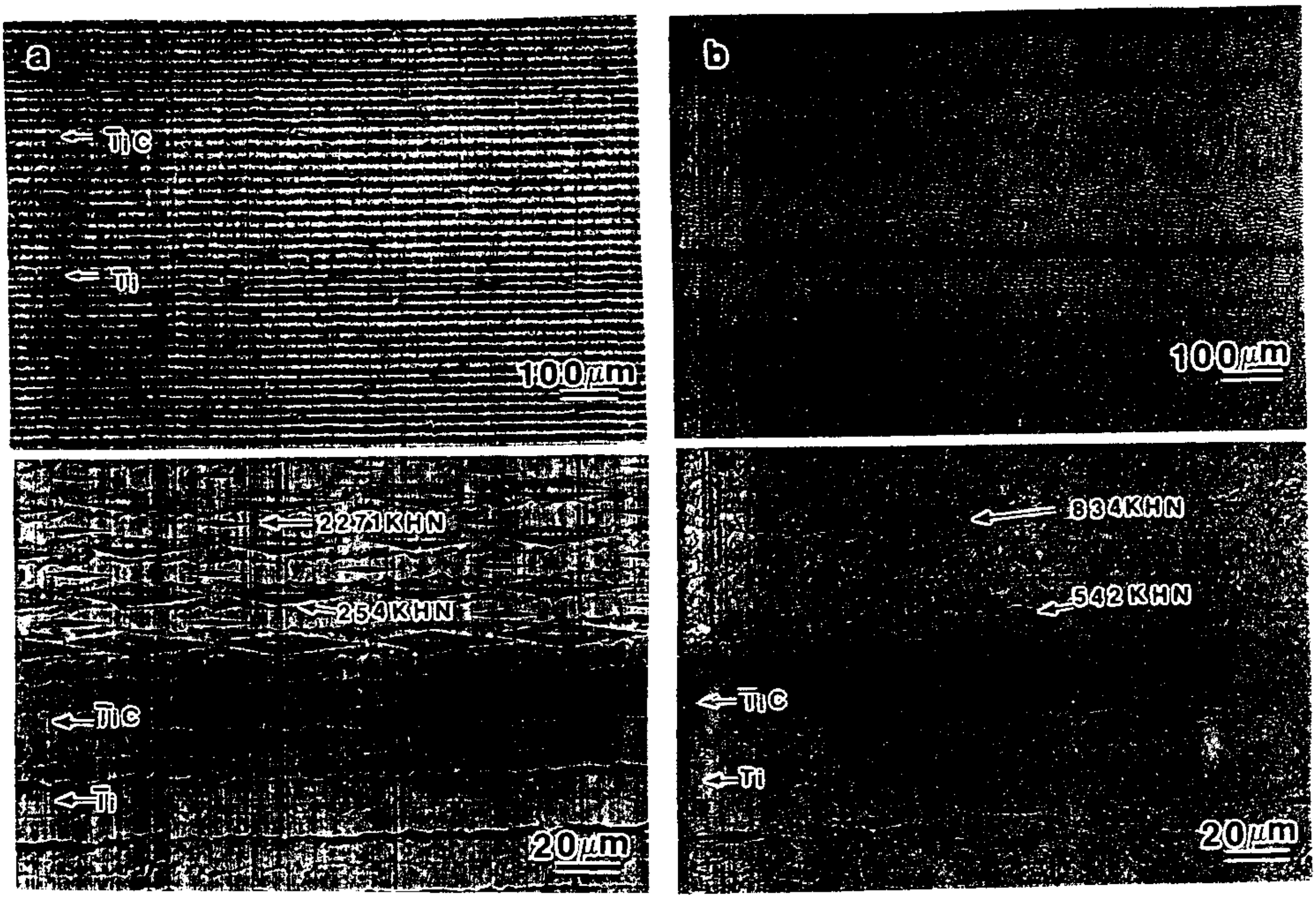

Microhardness on the cross-section (optical micrographs)

- thickness = 9 µm → H_{TiC} ≈ 22 to 23000 MPa ≡ to that of TiC layers
- épaisseur = 3 µm → H_{TiC} smaller (effect of adjacent layers)

Ti-TiC multilayer coatings (continued)

- **thickness of el. layers : (a) 9 µm; (b) 3 µm; (c) 1.25 µm (ded. from V_d)**
- **<u>Morphology</u> (scanning electron micrographs)**

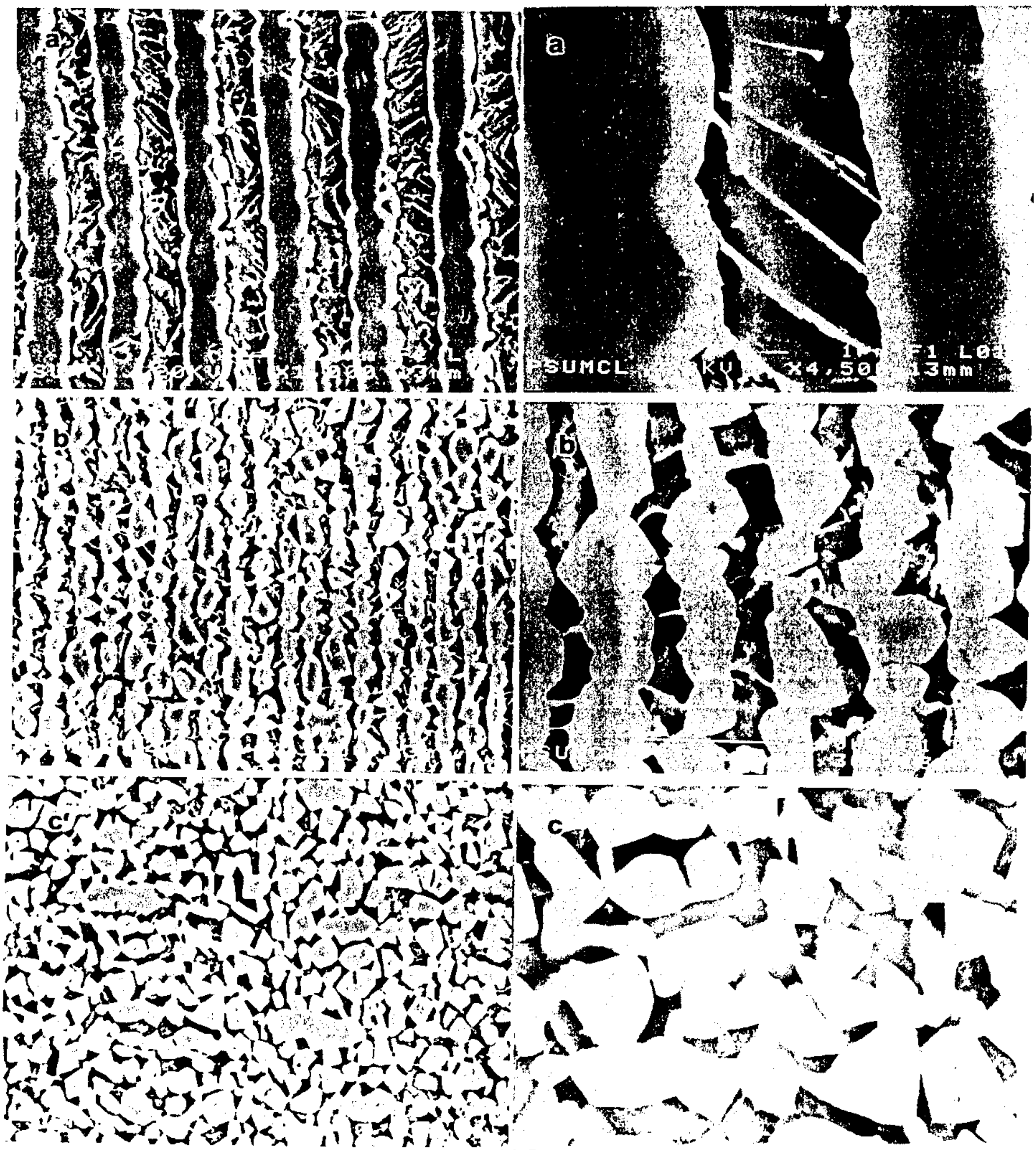

- **Clear zones = Ti ; dark zones = TiC**
- **With 1.25 µm → interdiffusion of materials at Ti/TiC interfaces**
- **thus : progressive shift from multilayer to composite coatings as thickness of elementary layers decreases**

Properties of EB-PVD coatings

- Structure (morphology)
- Mechanical properties of pure metal coatings (microhardness, tensile yield stress, …)
- Mechanical properties of composite coatings (dispersion-strengthened composites)
- Modeling of mechanical behavior of composite coatings
- Mechanical properties of particle-reinforced composite coatings
- Mechanical properties of multilayer coatings

Structure of metallic coatings produced by EB-PVD

- **Movchan - Demchishin Model**

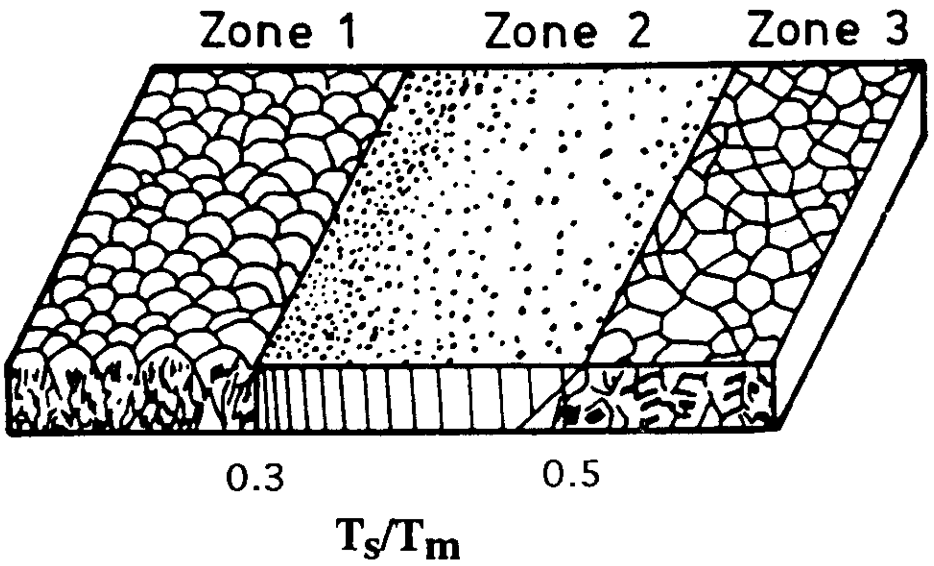

- **Thornton model**

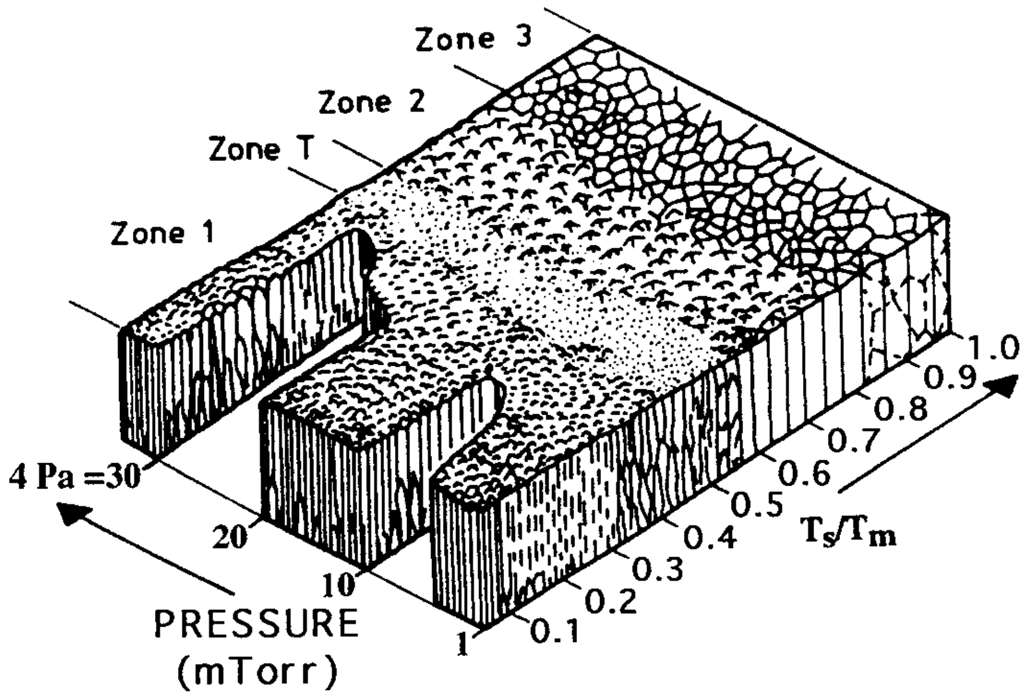

Mechanical properties of pure nickel coatings produced by EB-PVD

- thickness = 1 to 1.2 mm - deposition rate = 15 µm/min

- **Microhardness and tensile yield strength**

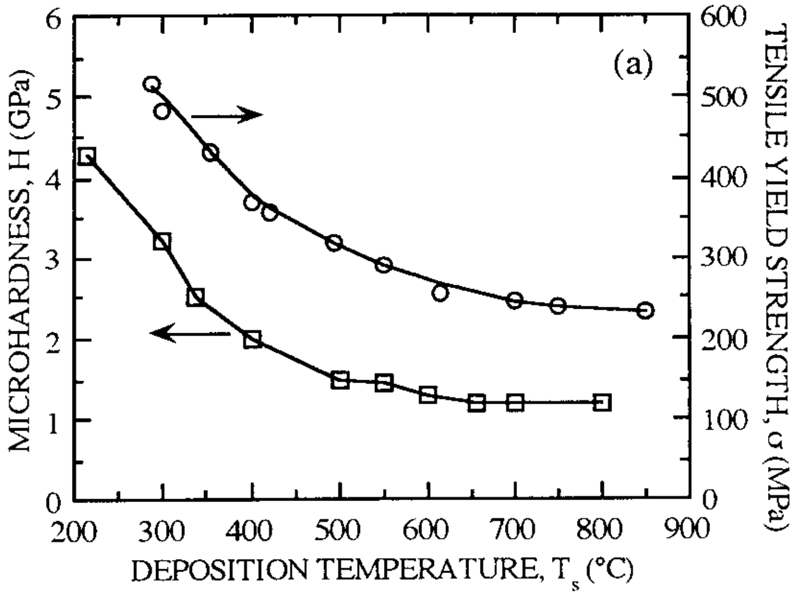

- **Elongation at rupture**

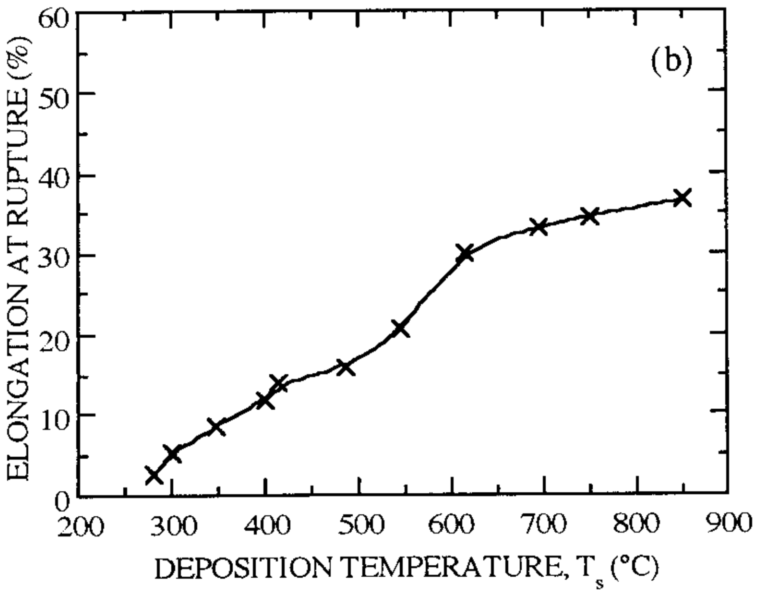

Mechanical properties of dispersion-strengthened composite coatings

- **Composition**

  - matrix : Fe, Ni (and others)
  - dispersed particles : Al_2O_3, ZrO_2, NbC, ZrB_2, (and others)
  - thickness : 0.8 to 2 mm

- **Major elaboration parameters**

  - deposition temperature
  - nature of the phase dispersed throughout the matrix

- **Deposition parameters**

  - deposition temperature = 0.5 to 0.8 T_m
  - deposition rate :
    - matrix : 4 to 14 µm/min
    - refractory compound (hard) : 0.2 to 1.5 µm/min

- **Physical characteristics**

  ○ grain size of the metallic matrix, D_g

  ○ diameter of dispersed particles, d

  - volume concentration of the dispersed phase, f

Structure of dispersion-strengthened composite coatings

- **<u>Grain size of the metallic matrix,</u> D_g**

in the plane perpendicular to the direction at which the vapor flux is incident on the substrate *<u>for PURE metals</u>* : Cu, Ni, ,Fe, W

$$D_g^2 = P \ \exp\left(-\frac{Q_g}{R\,T_S}\right)$$

- ❍ **Addition of dispersed particles → reduction in D_g (factor 10 for a volume fraction $f < 0.5$ %)**

- ❍ **Effect of interactions between phases at particle-matrix interfaces**

  (oxides → D_g is less than that for borides and carbides)

- ❍ **Proportionality factor, P, depends on f : $P \approx \left[\frac{1+\cos(\theta)}{f}\right]^m$**

$$D_g^2 = \left[\frac{1 + \cos(\theta)}{f}\right]^m \ \exp\left(-\frac{Q_g}{R\,T_S}\right)$$

- **The parameter $(1 + \cos\theta)$ was introduced into a formal description of the adhesion energy at the particle-matrix interface, similar to the adhesion energy at the interface of a refractory compound with a liquid metal**
- **$m = 0.5$ to 1**

Structure of dispersion-strengthened composite coatings (continued)

- **Mean particle size, d**

  - increases as the volume concentration increases

○ **Similar to the Lifshitz-Wagner relation (describing the growth rate of second phase particles in liquid and solid states of two-phase materials) :**

$$d^3 = \alpha_p f \ \exp\left(-\frac{Q_p}{R\,T_S}\right)$$

○ EXAMPLE : Ni-ZrO_2 system

- $Q_p = (27 \pm 3)$ kcal mol^{-1}
- $\alpha_p = 2 \times 10^{-9}$ cm^3
- with $f = 0.02$: $d \approx 20$ nm at $T_S = 650°C$

  $d \approx 120$ nm at $T_S = 1100°C$

- Porosity of coatings

  cavities of 5 to 10 nm for $T_S < 0.3\ T_m$

  larger porosity (cavities of 1 to 10 µm) depending on the type of particles, concentration of particles and temperature T_S

Mechanical properties of dispersion-strengthened composite coatings

- **Ni-ZrO_2 of 0.8 to 1.2 mm in thickness - (10 x 3) mm^2**
  T_S = 650, 850 et 1100°C → d = 150-200 to 1100-1300 Å
  - thermal annealing, 600°C/1h : samples 1, 2 and 3
  - thermal annealing, 1200°C/1h : samples 1a, 2a and 3a

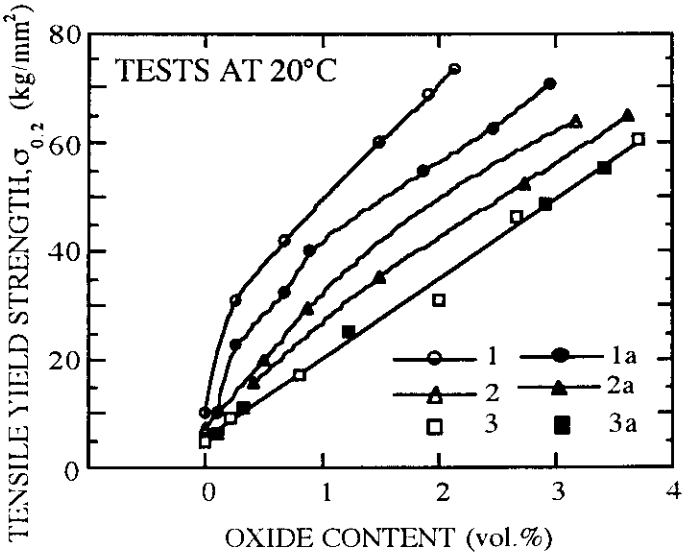

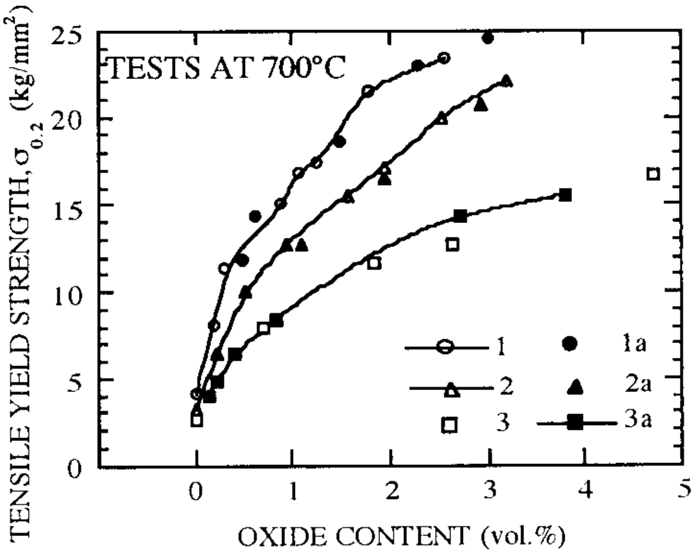

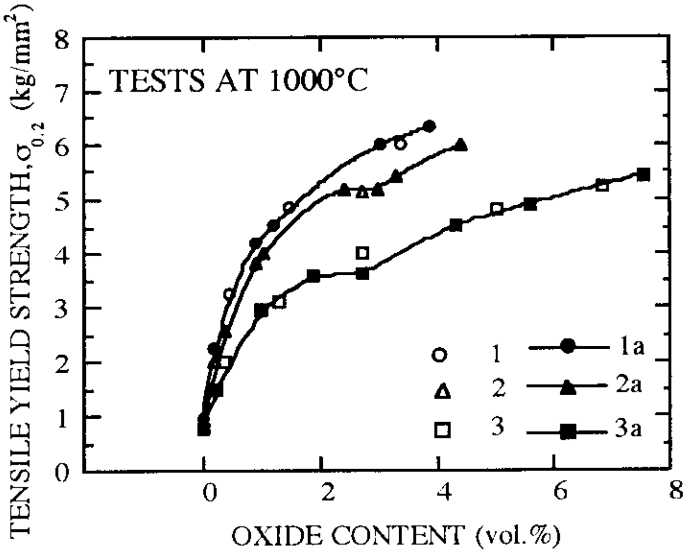

Mechanical properties of Ni-ZrO$_2$ composite coatings

- OROWAN-ASHBY MODEL

$$\sigma_{OR} = \sigma_m + 0.85\,\frac{G_m\, b_m}{2\,\pi\,\Lambda}\,\ln\left(\frac{d}{b_m}\right) \quad \text{or}$$

$$\sigma_{OR} = \sigma_m + 0.85\,\frac{G_m\, b_m}{4\,\pi\,(R_s - r_s)}\,\ln\left(\frac{r_s}{b_m}\right)$$

$2\,R_s = \sqrt{\frac{2\,\pi}{3\,f}}\;r_p$: mean planar center-to-center particle separation

$r_s = \sqrt{\frac{2}{3}}\;r_p$: mean planar particle radius in the slip plane

r_p : particle radius measured experimentally

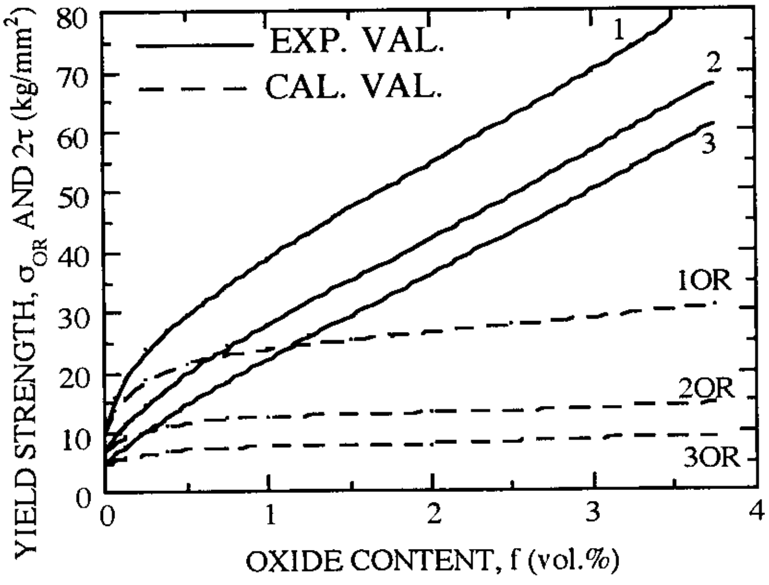

Mechanical properties of Ni-ZrO_2 composite coatings

- **MODELING (continued)**

- Deviation $\Delta\sigma = (\sigma_{0.2} - \sigma_{OR})$ increases linearly as f increases

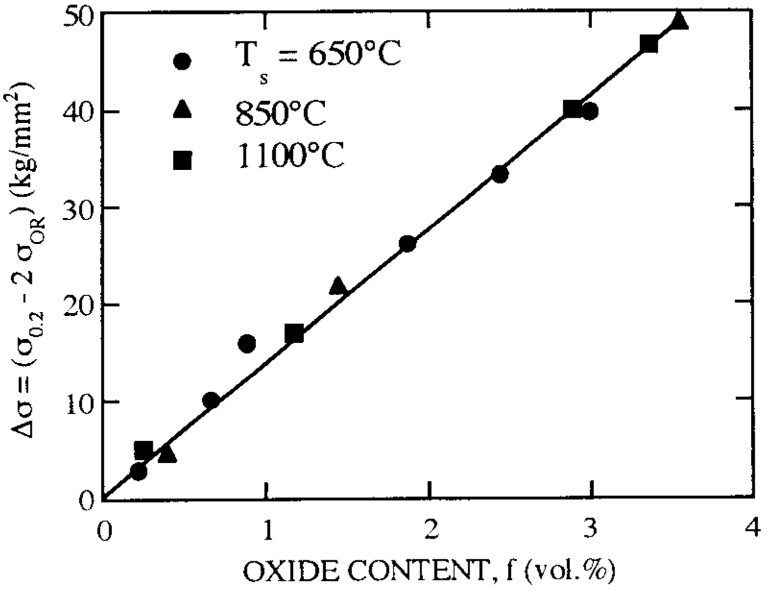

$$\Delta\sigma = K f$$

$K = 1.35 \times 10^3$ kg mm^{-2} - independent of r_p

$$\sigma_{0.2} = \sigma_{OR} + K f$$

Remarks :

- **expression is not valid for tests at high temp. (700 and 1000°C)**
- **effect of additional phenomena (thermally activated recovery processes, change in the mechanisms of plastic deformation and strengthening)**

Modeling of mechanical behavior of composite coatings

- **Model of Movchan et al.** (Simplified formulation)

$$\sigma_{0.2} = \sigma_{0m} + \alpha \frac{G_m b_m}{\Lambda}$$

$\frac{G_m b_m}{\Lambda}$ = Orowan stress

$\Lambda = \left(\frac{2d}{3f}\right)(1-f) \approx \frac{2d}{3f}$ thus :

$$\sigma_{0.2} = \sigma_{0m} + \beta \frac{G_m b_m}{d} f$$

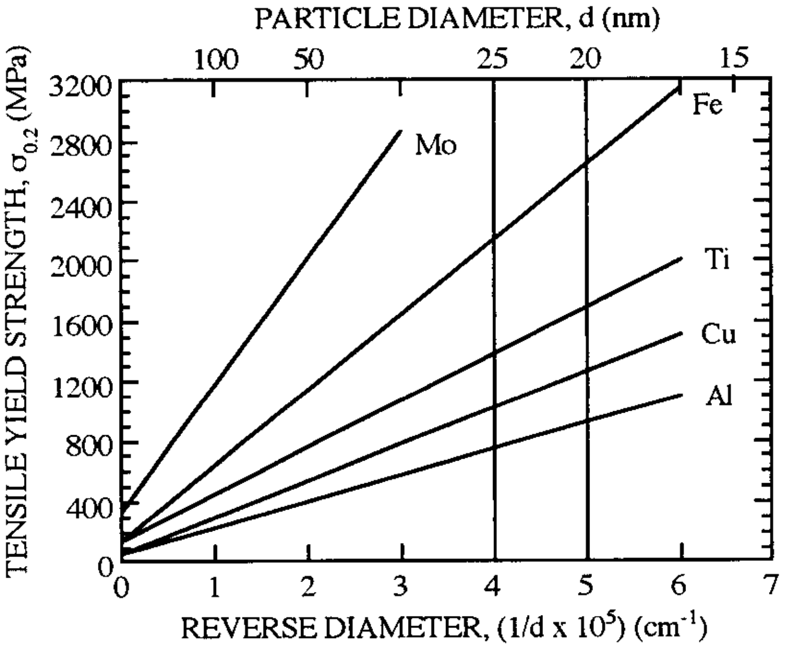

○ **Factor β = 38 to 60**

Estimation of $\sigma_{0.2}$ for coatings with d = 20 to 25 nm for which the ductility is convenient for various applications (elongation at rupture not below 2 or 3 %)

Modeling of mechanical behavior of composite coatings

- **Model of Movchan et al.** (continued)

  3 variants depending on the value of f or D_g/Λ

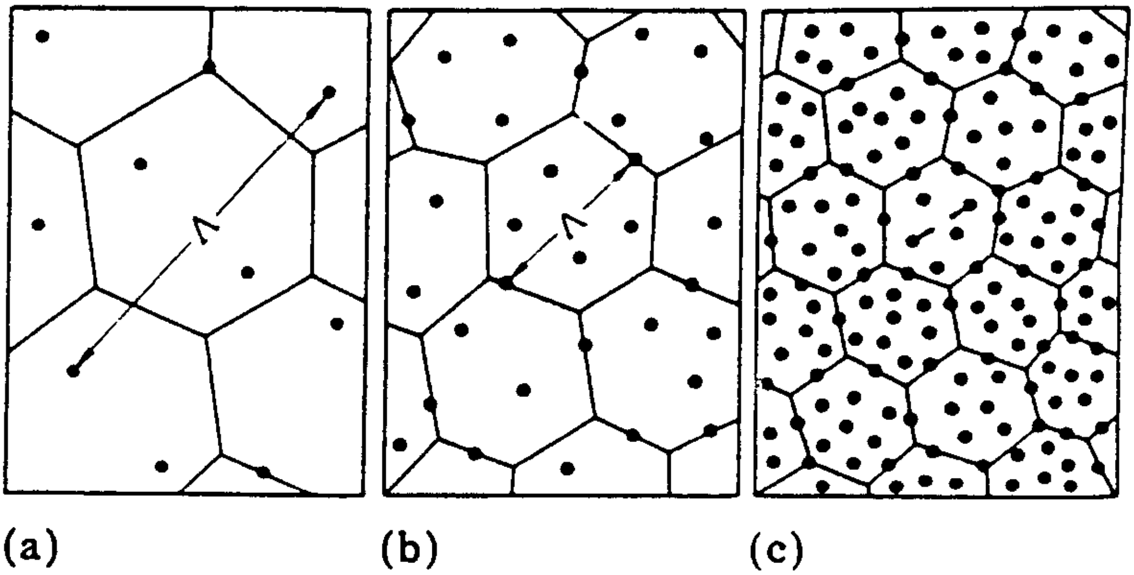

› Situation (c) more often investigated

- $D_g/\Lambda > 1$
- hard non-deformable particles

The yield strength is given by :

$$\sigma_{0.2} = \sigma_{0m} + \alpha \frac{G_m b_m}{\Lambda} = \sigma_{0m} + \beta \frac{G_m b_m}{d} f$$

Modeling of mechanical behavior of composite coatings

- **<u>Model of Movchan et al.</u> (continued)**

yield strength, $\sigma_{0.2}$ and elongation at rupture, δ

❍ ***hard non deformable particles (Fe-ZrO_2, Fe-NbC, W-ZrO_2) / deformable particles tightly adherent to the matrix (Ni-C, Fe-CaF_2)***

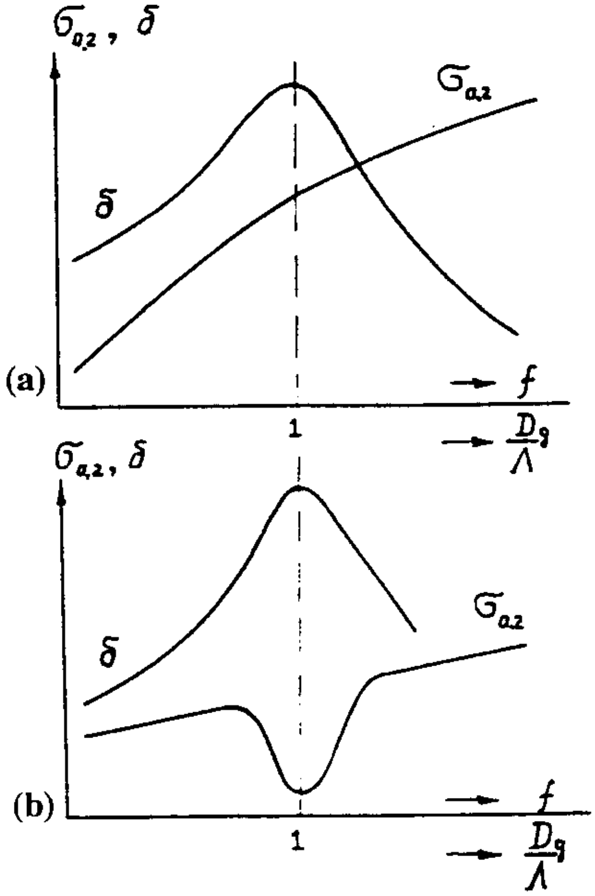

REMARKS :

1. **With $D_g/\Lambda < 1$ - if f increases, increase in σ more rapid for incorporation of hard particles with weak interactions with the matrix**
2. **With $D_g/\Lambda = 1$ - case (a), the strengthening effect is maintained**

case (b), decrease in strength but maximum ductility (1.5 to 2 times higher than the ductility of the pure matrix)

case (b), at high temp., elongation to rupture > 100 % → superductility

Mechanical properties of particle-reinforced composite coatings

- **<u>High particle content</u>** - f ≈ few ten vol.%

  - tensile yield stength, σ, max. for f = 60 to 80 vol.%
  - Λ ≈ λ (mean particle spacing)

$$\lambda = \left(\frac{2\ d^2}{3\ f}\right)(1 - f)$$

) EXAMPLE : Cu-Fe

yield strength, elongation at rupture

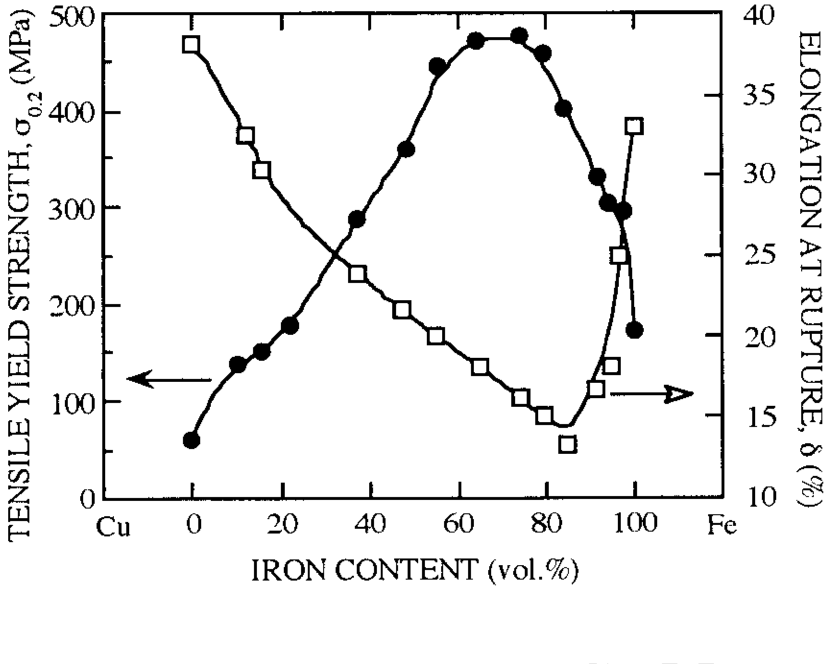

) OTHER EXAMPLES : Cu-Cr, Cu-Mo et Al-Be

- with 60 vol.% < f < 80 vol.%

$$\sigma_{0.2} = \sigma_{0p} + \frac{20\ G_p\, b_p}{d}\ f$$

Mechanical properties of Cu-Fe multilayer coatings

- **Microhardness of Cu-Fe multilayer coatings**

  - Palatnik et al., 1964-1967
  - thickness of samples = 15 to 25 µm
  - similar thickness, t, of (Cu or Fe) elementary layers
  - thickness, h, of Cu-Fe bilayers : $h = t_{Cu} + t_{Fe}$

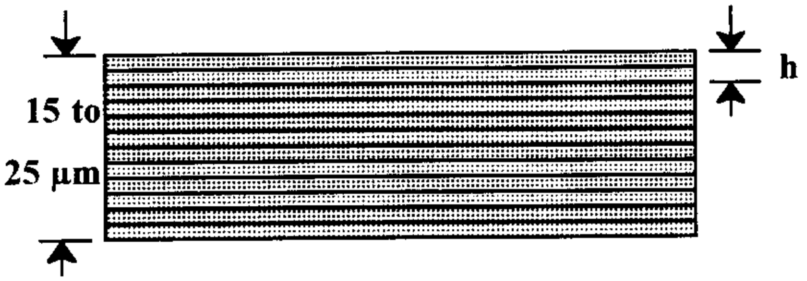

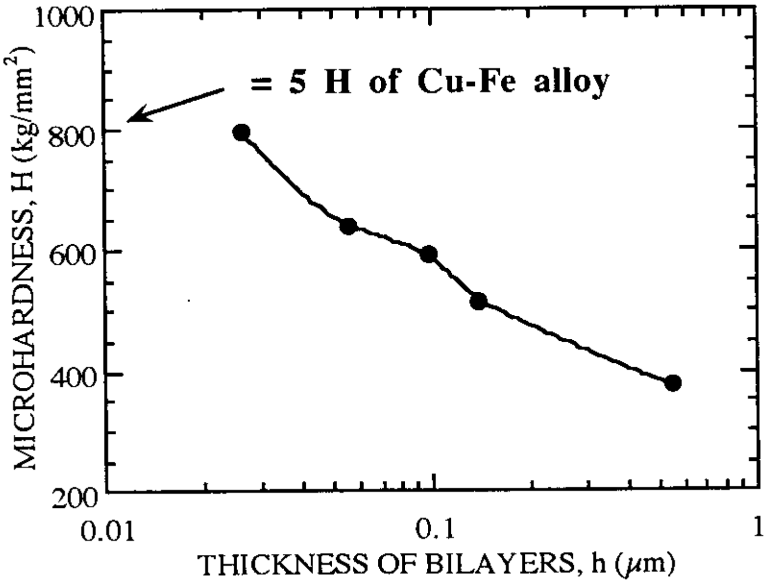

Mechanical properties of Cu-Fe multilayer coatings

- **Results of Palatnik et al.** **(continued)**

On the basis of the Hall-Petch relation

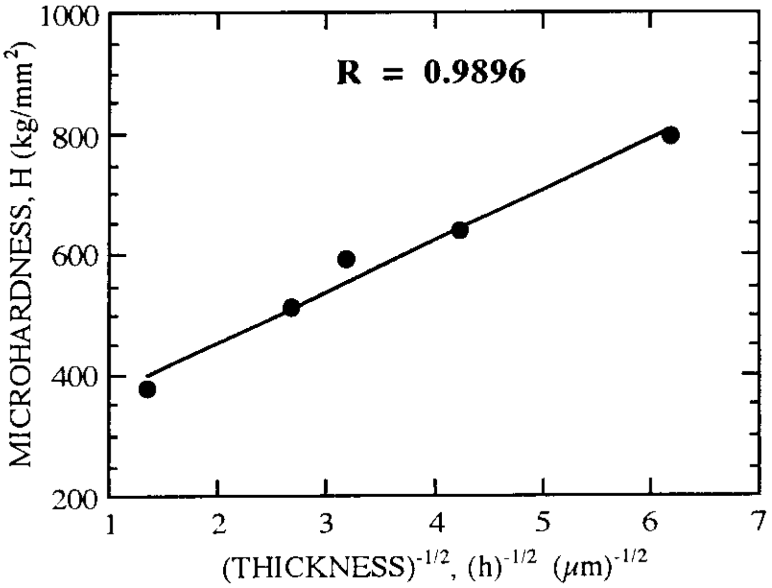

- **Other representation**

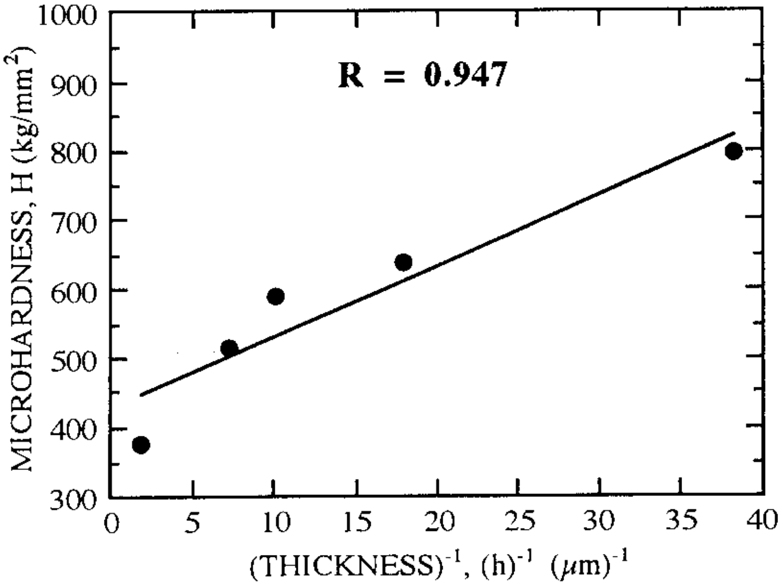

Mechanical properties of Fe-Cu multilayer coatings

- **Microhardness of Fe-Cu multilayer coatings**

  - Movchan et al. - Bunshah et al. (1980)
  - thickness of samples = 0.2 to 1 mm
  - thickness, t, of elementary layers

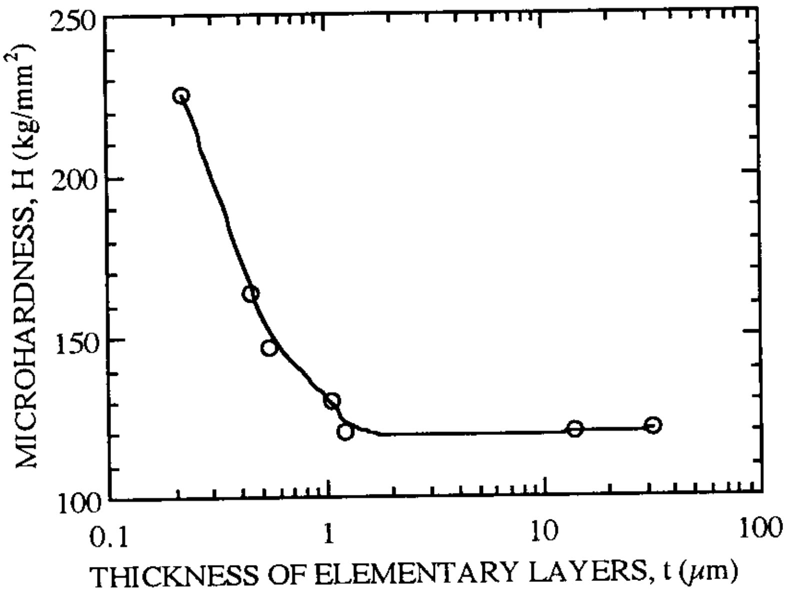

Mechanical properties of Fe-Cu multilayer coatings

- <u>**Results of Movchan et al. - Bunshah et al.**</u> **(continued)**

On the basis of the Hall-Petch relation

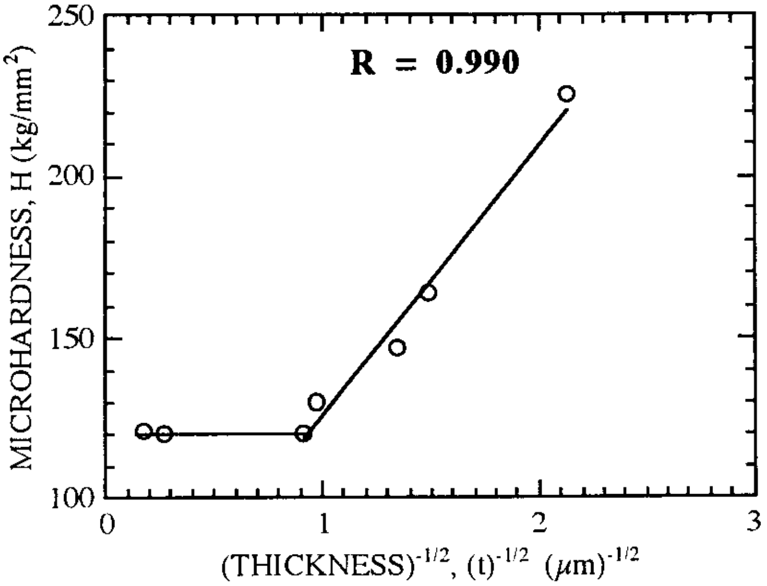

- <u>**Other representation**</u>

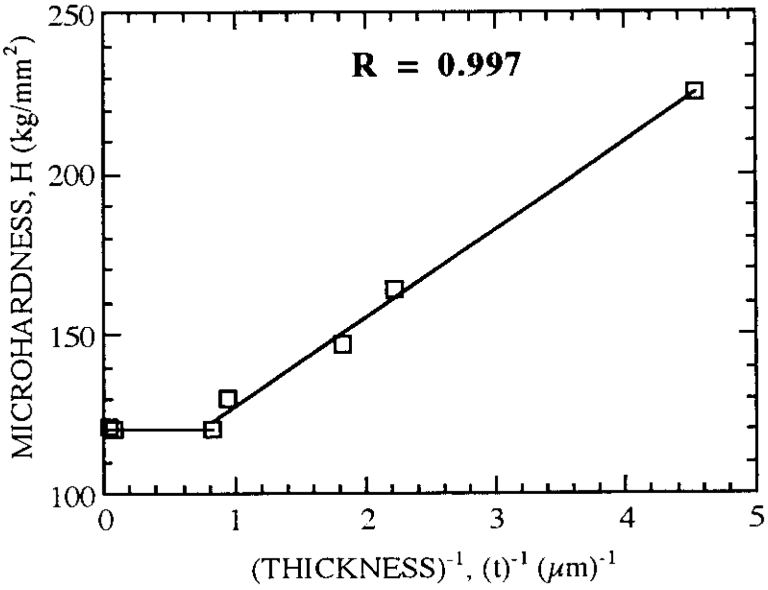

Mechanical properties of Cu-Mo multilayer coatings

- **Tensile yield strength of Cu-Mo multilayer coatings**

  - Movchan (1991)
  - thickness of the Mo elementary layer = 1.1 µm = constant
  - thickness of the Cu elementary layer = 7 µm or 5 µm or 1.8 µm
  - volume content of Mo, f = 0.38 ou 0.18 ou 0.13

Deposition temperature effect

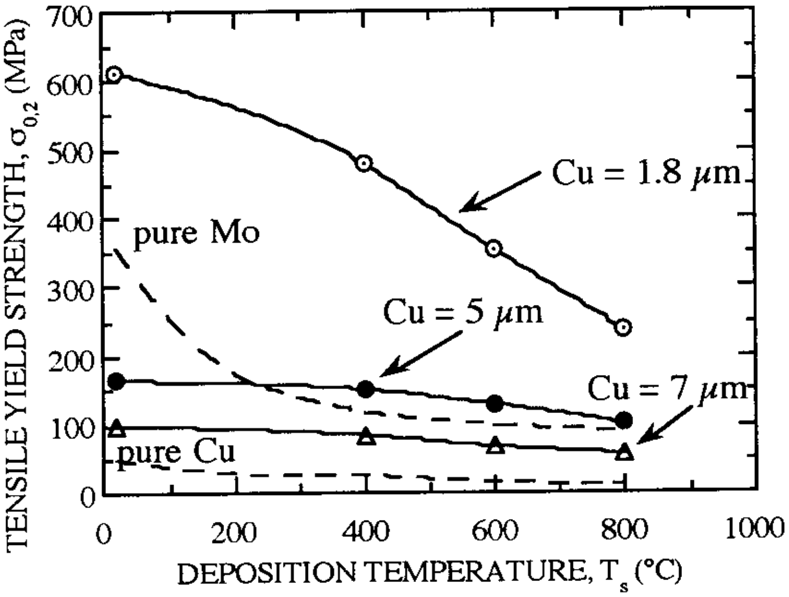

Mechanical properties of multilayer coatings

- **Model of Movchan**

  - Cu-Fe, Cu-Cr and Cu-Mo multilayer coatings
  - volume content of (Fe, Cr or Mo) addition element, $f > 0.5$

$$\sigma_{0.2} = \sigma_{0s} + \frac{30\, G_s b_s}{h} f$$

  - s : strenthening or reinforcement material ($G_s > G_m$)
  - h : thickness of reinforcement material elementary layer

- REMARKS :

1) Suitable selection of materials → multilayer stable at high temp.
   - for example, no interdiffusion
   - case of Cu-Fe, Cu-Cr and Cu-Mo multilayer coatings
2) Expression of $\sigma_{0.2}$ proposed by Movchan is not based on modeling of phenomena (for example, effect of grain boundaries on dislocation motion)
3) This expression is not related to the Hall-Petch relation
   - the relation in $1/(h)^{1/2}$ is disregarded while the relation in $1/h$ is used
4) This expression is similar to that proposed by Movchan for dispersion-strengthened composite coatings

expression of $\sigma_{0.2}$ for multilayer coatings is rather empirical or semi-empirical

Conclusions

- Mechanical properties (yield strength, hardness) of composite and multilayer EB-PVD coatings superior to those of single phase and monolithic coatings
- Modeling on the basis of models proposed for polycrystalline bulk materials :
  - ○ valid for dispersion-strengthened composite coatings
  - ○ no valid for multilayer coatings
- Fundamental investigations required for improved modeling of phenomena
- "Theoretical" limitations have no direct effect on the practical interest in EB-PVD process